N-terminal phosphorylation regulates the activity of Glycogen Synthase Kinase 3 from *Plasmodium falciparum*

Samuel Pazicky[1,2], Arne Alder[1,3,4], Haydyn Mertens[2], Dmitri Svergun[2], Tim Gilberger[1,3,4] and Christian Löw[1,2*]

[1] Centre for Structural Systems Biology (CSSB), Notkestrasse 85, D-22607 Hamburg, Germany.

[2] Molecular Biology Laboratory (EMBL), Hamburg Unit c/o Deutsches Elektronen Synchrotron (DESY), Notkestrasse 85, D-22607 Hamburg, Germany.

[3] Bernhard Nocht Institute for Tropical Medicine, Bernhard-Nocht-Strasse 74, D-20359 Hamburg, Germany.

[4] Department of Biology, University of Hamburg, Hamburg, Germany

*Corresponding author

Christian Löw

European Molecular Biology Laboratory Hamburg, Notkestrasse 85, D-22607 Hamburg, Germany.

Fax: +49 4089902149

Tel: +49 408998-87570

e-mail: christian.loew@embl-hamburg.de

https://orcid.org/0000-0003-0764-7483

Running title: N-terminal phosphorylation in PfGSK3

Keywords: malaria, GSK3, autophosphorylation, drug target, SAXS

Abstract

As the decline of malaria cases stalled over the last five years, novel targets in *Plasmodium falciparum* are necessary for the development of new drugs. Glycogen Synthase Kinase (PfGSK3) has been identified as a potential target, since its selective inhibitors were shown to disrupt the parasite`s life cycle. Here, we show that PfGSK3 exhibits autophosphorylation, leading to an extensive phosphorylation both *in vitro* and in the parasite. In the uncanonical N-terminal region of the parasite enzyme, we identified several autophosphorylation sites that regulate the activity of PfGSK3. By combining molecular modeling with experimental small-angle X-ray scattering data, we show that increased PfGSK3 activity is promoted by conformational changes in the PfGSK3 N-terminus, triggered by N-terminal phosphorylation. Our work provides novel insights into the structure and regulation of the malarial PfGSK3.

Introduction

Plasmodium falciparum is an intracellular eukaryotic parasite that causes the most severe form of malaria in humans, infecting over 200 million people every year (1). The emergence of malaria parasites resistant to all currently used antimalarial drugs imposes a serious threat to public health (2). Identification of new drug targets and drugs is therefore crucial for future handling of the malaria pandemics. Kinases comprise up to 10% of all drug targets (3) and a number of potent inhibitors were discovered that are directed against *P. falciparum* kinases, such as glycogen synthase kinase 3 (PfGSK3) (4). Human GSK3ß plays a crucial role in a number of signaling processes, regulating glycogen metabolism (5–7), cell cycle and growth (8–10), translation (7), embryonic development (9, 11) or differentiation of neurons (12–16). Consequently, the inhibitors of GSK3 are investigated as potential treatment options for neurodegenerative and psychiatric diseases (17–23) and its structure, catalytic mechanism and regulation are well studied (24–26). GSK3β is thought to be constitutively activated by autophosphorylation at Y216 (27–29) and inactivated by phosphorylation of N-terminal S9 mediated by several protein kinases, such as PKA and PKB (6, 30). The inactivation is achieved as the phosphorylated S9 enables binding of GSK3 N-terminus to a pocket for a priming phosphorylation in the substrate-binding region and thus reduces the binding affinity for substrates (24, 25).

In *P. falciparum*, two genes are encoding GSK3 (PF3D7_0312400 and PF3D7_1316000) and these enzymes are much less understood in their physiological role and in the molecular mechanism. GSK3ß (PF3D7_0312400, further as PfGSK3) is the only isoform that is expressed in blood stages (31) of the parasite and is involved in the regulation of red blood cell invasion (32). The invasion process is an essential, parasite-driven event that relies on the orchestrated interplay of multiple protein-protein interactions (33). It requires the apical membrane antigen 1 (AMA1), a type I transmembrane protein located in the micronemes of the parasite and translocated on its surface before the host cell entry (32, 34–39). The N-terminal ectodomain of AMA1 interacts with the rhoptry neck (RON) protein complex of the

parasite, that is inserted into the membrane of the red blood cell, forming the basis of the so called “tight junction” between the membrane of the invading parasite and its target cell (40–44). The short C-terminus of AMA1 locates inside the parasite and thus, is amenable to regulation by phosphorylation (45, 46). In a two-step phosphorylation event, protein kinase A (PfPKA) first phosphorylates S610 of AMA1 (45, 47, 48), which in turn enables subsequent phosphorylation of AMA1 residue T613 by PfGSK3 (32). Thus, PfGSK3 serves as a secondary kinase, although both phosphorylation sites are equally important for AMA1 function and *P. falciparum* invasion (32). PfGSK3 inhibitors, built on a thieno[2,3-b]pyridine or benzofuran scaffold, have been developed that display selective antiplasmodial activity with IC_{50} values in the low micromolar to sub-micromolar range (49–51) and one of these inhibitors has been shown to abrogate the red blood cell invasion (32). Further improvements of these inhibitors could be guided by a three-dimensional structure of PfGSK3 that has, however, not been determined so far.

Based on sequence homology across GSK3 proteins, PfGSK3 consists of two conserved structural domains: a β-sheet-rich lobe with an ATP binding pocket and an α-helical lobe with the activation loop and a substrate binding site. These domains are typically preceded by an N-terminal domain that is predicted to be disordered (25). In PfGSK3, the important residues in the ATP binding pocket and in the activation loop remain conserved, however, its N-terminus displays an unique extension and its function remains unknown (52).

To analyze this in more detail, we optimized the purification protocol of PfGSK3 that enabled us to perform thorough structural and functional characterization of the protein *in vitro*. We show evidence that PfGSK3 exhibits autophosphorylation of the N-terminal and activation loop residues *in vitro* and validated these phosphorylation sites *in vivo*. Phosphorylation of the N-terminal residues induces conformational changes of the protein that lead to an increase in the enzymatic activity of PfGSK3, providing a new regulatory mechanism.

Results

High yield expression and purification of enzymatically active PfGSK3 from *E. coli*

To obtain recombinant PfGSK3 in high purity and homogeneity that allow functional and structural analysis, we extended the previously established PfGSK3 expression and purification protocols (32, 49, 50, 53). In short, N-terminally hexahistidine-tagged PfGSK3 (Fig. 1A) was separated from the bacterial cell lysate by immobilized metal affinity chromatography (IMAC, Fig. 1B) and subsequent size exclusion chromatography (SEC, Fig. 1C). We deliberately excluded a negative IMAC step as PfGSK3 becomes sensitive to NiNTA beads upon the removal of the histidine tag and has a high tendency to precipitate. Instead, to remove the impurities, we included an additional ion exchange chromatography (IEC) step (Fig. 1D). This yields the desired level of purity of PfGSK3 as judged by SDS-PAGE, but the protein elutes in several partially overlapping peaks with increasing concentration of sodium chloride. Such heterogeneity of PfGSK3 might be caused by different posttranslational modifications. To assess the quality of the purified protein and to characterize it further, we applied several biophysical methods. Dynamic light scattering data confirm high homogeneity of the sample with a calculated molecular weight of 52 kDa, in agreement with the expected mass for a monomer of recombinant PfGSK3 (52.05 kDa, Fig. S2A). The secondary structure content derived from circular dichroism data is 22% α helix, 26% β sheet, 24% turns and 28% disorder. This corresponds to a typical domain organization of homologous GSK3 proteins (such as human GSK3β) with an N-terminal β-sheet-rich domain and an α-helical C-terminal domain that are flanked by disordered N-terminal and C-terminal regions (Fig. S1A, Fig. 2A) (24, 54). To verify that the protein retains its three-dimensional structure and kinase properties, we tested whether its thermal stability changes in the presence of ATP and ATP analogs. Indeed, the stability of PfGSK3 markedly increased in a concentration dependent manner from 45°C to over 50°C with increasing concentration of dATP or ATP (Fig. 2B and Fig. S2B). Moreover, the protein could also be stabilized by several non-hydrolysable ATP analogs (Fig. S2C). Additionally, we observed a concentration-dependent increase of the thermal stability of

PfGSK3 with increasing concentrations of sulfate ions (Fig. S2D-E). Sulfate ions are bound in the activation loop of several human GSK3 structures (55–61), suggesting that the structural elements in this region are also conserved. Finally, we measured the PfGSK3 activity with a luciferase assay, using a peptide derived from human glycogen synthase 1 (GS-1) as a substrate, resulting in a catalytic rate constant of k_{cat} = 9.5 s^{-1}, which is in a similar range as previously reported (between 0.7 and 3.7 s^{-1}) for human GSK3 (Fig. 2C, Fig. S2F) (54). Thus, purified PfGSK3 is folded, stable, enzymatically active and retains the structure that is expected to be similar to human GSK3.

Divalent ions of heavy metals induce reversible formation of PfGSK3 oligomers

The observation that PfGSK3 after affinity tag cleavage has a strong tendency to precipitate upon interaction with NiNTA beads prompted us to investigate the impact of various heavy metals on PfGSK3. To this end, we measured the thermal unfolding profiles of the protein in the presence of different metal ions. Under standard conditions, PfGSK3 displays a clear transition midpoint at 45°C. However, in the presence of divalent ions, such as zinc, cobalt, nickel and copper cations, the typical unfolding transition profiles completely disappear, indicating structural changes (Fig. S3A). We selected zinc to investigate further the effect of divalent heavy metal ions on PfGSK3 because it showed the most pronounced effect on PfGSK3 unfolding. Interestingly, the secondary structure content measured by circular dichroism did not notably change upon addition of zinc, demonstrating that the secondary structural elements of the protein remain folded (Fig. S3C). However, analytical size exclusion chromatography revealed that the zinc cations induce the formation of high molecular weight (high-MW) protein species that elute earlier from the column than the metal-free protein (Fig. 3A) and this effect is dependent on the concentration of the zinc cations (Fig. S3B). Indeed, in a cross-linking experiment with glutaraldehyde, the high-MW species appear predominantly in the presence of zinc (Fig. S3D). The high-MW species can revert to monomers by the addition of the divalent metal chelator EDTA (Fig. 3A). To study the impact of heavy metals on the PfGSK3 function, we measured its activity in presence of zinc at different

143 concentrations. The metal cations cause a dramatic decrease in the PfGSK3 activity (Fig. 3B).
144 However, the activity is completely restored after EDTA treatment. Finally, we used
145 small-angle X-ray scattering (SAXS, Fig. 3C and Fig. S3E) and negative stain EM (Fig. S3F)
146 to characterize the high-MW species. The distance distribution derived from the SAXS data
147 demonstrates high anisometry of the particles (peaking at 20 nm but with D_{max}=90 nm). In
148 agreement, the cross-linked high-MW species visualized by negative stain EM vary in their
149 shape and size (Fig. S3F). In summary, heavy metal ions, such as zinc cations, induce a
150 reversible formation of large PfGSK3 particles. While the protein maintains its secondary
151 structure, it completely loses its enzymatic activity. Importantly, the process is reversible and
152 the restored PfGSK3 monomers fully regain their kinase activity.

153 **PfGSK3 exhibits autophosphorylation**

154 PfGSK3 elutes from the IEX chromatography column in at least four different species with
155 distinct elution volumes that are of comparable purity (Fig. 1D). Such behavior could be
156 explained by a heterogeneous phosphorylation pattern. To investigate this possibility, we
157 separately analyzed the four top peak fractions (F1-F4) from the IEX elution profile of the wild
158 type PfGSK3 preparation (Fig. 1D). SDS-PAGE stained with the Pro-Q Diamond stain, which
159 specifically binds to phosphorylated proteins, shows that the amount of total phosphorylation
160 increases towards later elution volumes (Fig. S4A). Mass spectrometry analysis revealed that
161 the protein is partially phosphorylated at multiple sites. We identified a number of
162 phosphorylated residues at the N-terminus (residues 13-62, see Fig. S4B). Additionally,
163 several residues in the activation loop, primarily S226 and Y229, but also S228 and S232 were
164 found to be phosphorylated (Fig. S4B). The phosphorylation of the activation loop residues
165 and two N-terminal serine residues (S31, S62) is in agreement with the previously identified
166 phosphorylation sites in *P. falciparum* blood-stage parasites (37–39, 62–65), while the
167 phosphorylation of other N-terminal residues, predominantly Y39, S40, S42 and S43, has not
168 been detected in parasite lysate-based phospho-fingerprinting. As the *E. coli* expression
169 system only possesses a limited capacity to phosphorylate proteins (66–68), we tested the

ability of PfGSK3 to exhibit autophosphorylation by incubating recombinant protein with ATP/$MgCl_2$ and subsequent analysis of the ion exchange chromatography profiles. Indeed, the treatment with ATP/$MgCl_2$ led to a drop in the fluorescence signal from the earlier eluting peaks and gain in the fluorescence signal from later eluting peaks, indicating that PfGSK3 is able to exhibit autophosphorylation *in vitro* (Fig. 4A). In addition, we employed the luciferase activity assay to examine PfGSK3 activity in the absence of a substrate peptide. The assay showed the consumption of ATP even in the absence of the substrate peptide that was dependent on the concentration of PfGSK3, confirming that PfGSK3 exhibits autophosphorylation (Fig. 4B).

The N-terminus of endogenous PfGSK3 is phosphorylated

Having observed autophosphorylation of PfGSK3 *in vitro*, we also investigated the phosphorylation state of PfGSK3 expressed in the parasite. To this end, we made use of a *P. falciparum* cell line endogenously expressing C-terminally GFP-tagged GSK3 (GSK3-GFP, Fig. S5). The parasites were harvested at the schizont stage and GSK3-GFP was purified using GFP Trap agarose beads (Fig. 5A) and subjected to mass spectrometry analysis. The identified peptides exhibited phosphorylation both at the N-terminus and in the activation loop, similarly to recombinantly expressed PfGSK3 (Fig. 5B). The generally low Mascot Delta Score (69) did not allow us to confidently pinpoint the exact phosphorylation sites, but confirmed that a significant portion of the residues on the peptide derived from the unstructured N-terminus were phosphorylated (average 28%, residues 39-43) compared to the activation loop peptides (average 5%, residues 226-233). These data attest that N-terminal phosphorylation of PfGSK3 also occurs *in vivo.*

N-terminal domain is indispensable for PfGSK3 stability

To investigate the role of phosphorylation in PfGSK3 further, we attempted to express inactive mutants to prevent autophosphorylation. Therefore, we changed the essential residue in the ATP binding pocket K96 or residues from the activation loop S226 and Y229 to alanine. The

196 small-scale expression screen showed that the inactive mutants of PfGSK3 did not express in
197 a soluble form but instead formed inclusion bodies (Fig. 6A). We then isolated the inclusion
198 bodies of the PfGSK3^{K96A} and PfGSK3$^{S226A/Y229A}$ mutants and examined their phosphorylation
199 states by mass spectrometry. These mutants display the full length sequence but are devoid
200 of any phosphorylation (K96A) or exhibit markedly reduced phosphorylation (S226A/Y229A)
201 compared to the wild-type protein (Fig. 6C). This indicates that these mutations either impair
202 PfGSK3 function or PfGSK3 phosphorylation is crucial for folding and solubility. The latter is
203 further supported by a co-expression experiment of wild-type PfGSK3 with the
204 dephosphorylating lambda phosphatase, which results in insoluble material only (Fig. S6C).
205 As we found the N-terminal extension of PfGSK3 to carry several phosphorylation sites, we
206 cloned a series of N-terminally truncated protein constructs (Fig. S1A). None of these
207 constructs expressed in a soluble form (Fig. 6B) and mass spectrometry confirmed a complete
208 lack of phosphorylation in the PfGSK3 activation loop (ΔN64 in Fig. 6C). Expression tests at
209 different temperatures indicate that not only the aforementioned mutants and constructs, but
210 also wild-type PfGSK3 is less expressed and mainly insoluble at lower temperatures. In fact,
211 constructs with truncated N-termini did not express at 18°C at all, and even the wild-type
212 protein forms only inclusion bodies under such experimental settings (Fig. S6A-B). These data
213 further stress the crucial role of the PfGSK3 N-terminus as well as its phosphorylation sites for
214 folding and function of PfGSK3. As the N-terminally truncated PfGSK3 constructs are devoid
215 of any phosphorylation, we propose that the N-terminal PfGSK3 domain, unique for
216 *Plasmodium* species, is essential for PfGSK3 stability.
217

218 **N-terminal phosphorylation fine-tunes the activity of PfGSK3**

219 Provided that the PfGSK3 N-terminus is indispensable for its function, we suspected that this
220 region could also be a potential site of PfGSK3 regulation, as it is in human GSK3β. Therefore,
221 we analyzed the individual separated fractions from IEX chromatography (Fig. 1D) by
222 LC/MS-MS. Here, we observed that the extent of phosphorylation of residues in the activation

loop of PfGSK3 is comparable between the four fractions, but large differences in the N-terminal phosphorylation patterns are obvious (Fig. 7A). Specifically, all N-terminal residues are significantly less phosphorylated in the first fraction (F1), while in the second fraction (F2), the extend of phosphorylation of residues Y39 and S40 is strongly increased and the third and fourth fractions (F3 and F4) have generally higher level of N-terminal phosphorylation, which is most pronounced on residues Y39, S40, S42 and S43. Of note, only residue S40 is well conserved across *Plasmodium* species, but all other *Plasmodium* species contain multiple non-conserved N-terminal residues that are potential phosphorylation sites (Fig. S7A, F). To assess the relationship between the activity of PfGSK3 and its phosphorylation pattern, we made use of the differences in N-terminal phosphorylation between the individual IEX fractions and measured their kinase activity separately (Fig. 7B). PfGSK3 activity rises with an increase in N-terminal phosphorylation levels (from F1 to F4), supporting that phosphorylation is crucial for activity. Phosphorylation levels of residues S40, S42 and S43 significantly correlate with the PfGSK3 activity (Pearson $R=0.6$, $p<0.05$ in all cases, Fig. 7C-E), while this correlation is absent or insignificant for the other residues (Fig. S7B-F). These data support the hypothesis that phosphorylation of N-terminal PfGSK3 residues enhances PfGSK3 activity.

N-terminal phosphorylation affects the PfGSK3 structure

The phosphorylated residues at the PfGSK3 N-terminus are, based on structural homologs (24, 25), expected to be distant from the active site of the protein and it is therefore unclear how N-terminal phosphorylation regulates the protein activity. In the human counterpart, the phosphorylation of S9 prompts the binding of the N-terminus to a pocket for a priming phosphorylation in the substrate-binding region and reduces the binding affinity for substrates (24, 25). Hence, we investigated structural consequences of N-terminal phosphorylation in PfGSK3. Circular dichroism data on the least (F1) and most (F4) phosphorylated fractions show no pronounced differences in their secondary structure content (Fig. 8A). Thus, to investigate the impact of the N-terminal phosphorylation on the tertiary structure of PfGSK3, we used the *de novo* structure prediction server Robetta and the TrRefineRosetta method (70)

to generate initial PfGSK3 models that were further fitted against the SAXS data measured on separated PfGSK3 IEX fractions F1 and F4 (Table 1, see Fig. 1D). Using the wild type PfGSK3 sequence as well as PfGSK3 sequences with phosphomimetic mutations (see Methods), we generated 25 models (Fig. 8A) that display similar structure of the core domains but are structurally diverse in both termini (Fig. 8A). We identified a subset of models that provide the best fits to the experimental SAXS data (Table 1, Fig. S8B) of fractions F1 or F4 (Fig. 8D). Overall, the models with a larger radius of gyration (see the point sizes in Fig. 8D) display lower χ^2 (goodness-of-fit) values. Further refinement of these best-fitting extended models was conducted in the program CORAL (71) that enables assigning additional flexibility to existing models (Fig. 8E,H). This approach led to poorer fits when only C-terminus (residues 403-440) or both N-terminus and C-terminus (residues 1-64 and 403-440) were assigned flexibility (Fig. 8E,H). However, conducting refinement with a disordered C-terminus (residues 403-440) and a flexible stretch of residues between the N-terminus and the PfGSK3 core (residues 47-63, conformation B, Fig. 8E,H) led to two refined models displaying lower χ^2 values compared to the SAXS data from fraction F4. Ultimately, for both fractions, the models with the lowest χ^2 values display α-helical structure at the N-terminus. This α-helix is extended in the less phosphorylated F1 fraction (Fig. 8B) and folds back in the more phosphorylated F4 fraction (Fig. 8C). The raw SAXS data support such conformational differences, as both the calculated radius of gyration R_g and maximum intra-particle distance D_{max} decrease from F1 to F4 fraction (R_g 3.4 vs 3.2 nm; D_{max} 13 vs 12 nm, respectively, see Table 1). The dimensionless Kratky plot data representation also suggests a more extended conformation for the F1 fraction (Fig. S8C), as the F1 curve broadens and shifts to higher sR_g values relative to F4. The refined models fit the SAXS data well (χ^2 values of 1.19 and 1.06, respectively, Fig. 8F,G), but should be viewed cautiously as an average representation of the conformations present in solution that contains a mixture of differently phosphorylated species. In conclusion, the combinatorial approach indeed shows that upon phosphorylation, PfGSK3 becomes more flexible, enabling a conformational change in the N-terminus. This change presumably mediates the increased PfGSK3 activity upon phosphorylation.

Discussion

Identification and characterization of novel drug targets in malaria remain an important goal as drug-resistant parasites are a persisting threat in the fight against malaria. PfGSK3 has been identified as a potential drug target since its inhibitors also possess potent and selective anti-plasmodial activity. Understanding its function is therefore important for further improvement of these inhibitors.

Here, we have shown that PfGSK3 is expressed in *E. coli* as a folded and functional protein with a heterogeneous phosphorylation pattern. We assume that the heterogeneity originating from this diverse phosphorylation is the main reason why we were not able to grow PfGSK3 crystals for detailed structural characterization (72). Moreover, the PfGSK3 C-terminus, predicted to be disordered, and its unusual N-terminus represent additional challenges in protein crystallization. As the expression of inactive PfGSK3 protein (K96A, S226A, Y229A) as well as the removal of heavily phosphorylated N-terminus result in insoluble protein that lacks phosphorylation, other protein constructs and strategies will likely need to be considered for the structure determination of PfGSK3 in the future. At the same time, these results highlight the importance of both PfGSK3 phosphorylation and the necessity of an intact N-terminus for protein stability.

Our mass spectrometry analysis of the phosphorylation pattern on recombinant PfGSK3 confirmed a number of PfGSK3 phosphorylation sites known from previous phosphoproteomics studies (S31, S62, S226, S228, Y229, S232) (37–39, 62–65). The additional phosphorylation sites at the N-terminus (Y39, S40, S42 and S43) might have occurred due to the heterologous expression, but could also hint towards additional phosphorylation sites present *in vivo* under certain conditions. In general, these phosphorylation sites are reminiscent of those identified in human GSK3β. In GSK3β, the autophosphorylation of Y216 in the activation loop is thought to maintain the constitutive activity of the protein (27, 29), while phosphorylation of N-terminal S9 by other kinases, such as PKA and PKB, inhibits the enzyme (6, 30). Although the role of the activation loop

autophosphorylation is likely conserved between the human and *P. falciparum* proteins, the role of N-terminal phosphorylation seems to be different.

First, the N-terminal sequence is not conserved between the two homologous proteins, with *Plasmodium* species displaying an unusual extension with a number of potential phosphorylation sites. Second, whereas N-terminal phosphorylation of S9 in human GSK3 is mediated by other kinases, the phosphorylation of N-terminal residues in PfGSK3 is the result of autophosphorylation, as we show here. Last, while phosphorylation of S9 in human GSK3 inhibits its activity, our work illustrates that the increasing amount of phosphorylation on the PfGSK3 N-terminus results in an increased enzymatic activity.

Our structural investigation using the combination of structure prediction and its validation using experimental SAXS data provides further insights into how the N-terminal phosphorylation affects PfGSK3 structure. Two SAXS datasets originating from two differently phosphorylated IEX fractions of PfGSK3 directed the modelling towards PfGSK3 conformations with an α-helical N-terminus in both cases. However, this helix extends away from the active side of PfGSK3 in the less phosphorylated fraction, or folds back towards the center of the protein in the more phosphorylated fraction. It is possible that the “folded back” conformation (Fig. 8C) could be mediated by an N-terminal intramolecular coiled-coil interaction induced by phosphorylation, as the probability of coiled-coil formation increases with the increasing number of N-terminal PfGSK3 phosphomimetic mutations *in silico* (Fig. S8D). Interestingly, human GSK3β undergoes a similar conformational change, where upon phosphorylation of S9, its N-terminus binds in its substrate-binding region and competitively inhibits its activity (24, 25). However, N-terminal phosphorylation of PfGSK3 leads to an increase in enzymatic activity, suggesting a different regulatory mechanism. The conformational change upon phosphorylation might position the very N-terminus of PfGSK3 close to its core domains, potentially enabling intramolecular interactions that could enhance its activity. Alternatively, the N-terminal extension might interact with the substrates to guide them to the PfGSK3 active site. In both cases, the conformational change would be driven by

phosphorylation of residues 39-43, whereas the interacting residues are possibly confined to the very N-terminus (residues 1-20) that is conserved in *Plasmodium* species (Fig. S6A,F). It should be noted that the N-termini of PfGSK3 homologues are not well conserved even among the representatives of *Apicomplexa*; however, a number of residues that can be phosphorylated could still enable a similar mode of regulation as we have described here (Fig. S7A,F). Indeed, S33 of *Plasmodium berghei* GSK3 (PBANKA_0410400), equivalent to S40 in PfGSK3, was found to be phosphorylated in early gametogenesis (73). Residues equivalent to S40 of PfGSK3 are conserved across all *Plasmodium* species and residues that can be phosphorylated are also present in the vicinity of S40 in most *Plasmodium species* (equivalent to residues 38, 39 and 42 in *P. falciparum*), suggesting that the mechanism of regulation *via* N-terminal phosphorylation is preserved in all *Plasmodium* GSK3 proteins.

We have shown that this N-terminal phosphorylation, as well as the phosphorylation of the activation loop, are the result of PfGSK3 exhibiting autophosphorylation. This result confirms data in a recent publication, where the authors suspected that a high background in their phosphorylation assay could be attributed to autophosphorylation (74). Autophosphorylation of human GSK3β occurs directly after protein synthesis while the protein is associated with chaperones, such as HSP90 (27). Interestingly, a major contaminant during our PfGSK3 purification process was *E. coli* DnaK that shares 48-57% identity with various *P. falciparum* Hsp70 proteins, indicating that chaperone-assisted autophosphorylation might be conserved across these taxa. Moreover, PfGSK3 was less soluble and had lower expression levels at lower temperatures (25°C and 18°C), at which the chaperone levels in *E. coli* are also reduced (75). This further supports that chaperons could be crucial interaction partner for the first stages of PfGSK3 autophosphorylation, which are likely crucial for its solubility.

Additionally, we have revealed another means of PfGSK3 regulation: the divalent heavy metal ions, such as zinc and copper, inhibit the activity of PfGSK3 by inducing the formation of heterogeneous high-MW particles. The ionic radii of these cations are in a small range of 1.09-1.21 Å, indicating that the effect is mediated through a specific binding site. The fact that the protein becomes more sensitive to the metal ions only after the cleavage of the N-terminal

affinity tag indicates that this potential binding site could be located in close proximity to the N-terminus of PfGSK3. Indeed, a partially overlapping set of divalent cations inhibiting human GSK3β can be found in the literature, including lithium, beryllium, zinc, copper and mercury (17, 76, 77). Lithium and beryllium ions inhibit GSK3 by competing with magnesium ions that mediate ATP binding (77–79), but to our knowledge, they have not been shown to induce the formation of high-MW particles. To this date, there has been no structure of a GSK3 homolog with a bound heavy metal ion deposited in the PDB database, and thus the inhibition mechanism of heavy metal cations remains unknown. Importantly, as the high-MW particles can dissociate back into active PfGSK3 monomers, it cannot be excluded that this type of regulation is applied *in vivo*. The concentration of zinc in *Plasmodium* cytosol peaks at the late blood stages and should be sufficient to induce the formation of high-MW PfGSK3 species (80). Moreover, the concept of “auto-inhibitory polymerization” has already been described in detail for human CK2 (81), further underlining the possible similarities between PfCK2 and PfGSK3. It remains to be evaluated experimentally *in vivo* whether the PfGSK3 high-MW particles play a role in its native environment.

In conclusion, our work provides new insights into the function of PfGSK3 and its regulation by N-terminal phosphorylation and heavy metals, highlighting that phosphorylation influences the structure of the PfGSK3 N-terminus that in turn results in increased kinase activity.

Experimental procedures

Cloning and mutagenesis

The vector with N-terminally His-tagged PfGSK3 was generated by PCR amplification of the GSK3 coding sequence from *P. falciparum* cDNA followed by Ligation Independent Cloning into HindIII/KpnI-cleaved plasmid pOPIN F (82) using the In-Fusion HD EcoDry Cloning Kit (Takara Clontech) according to the manufacturer's instructions. The mutants S226A, Y229A and S226A/Y229A were generated by overlap extension PCR amplification from the original vector and Ligation Independent Cloning as described above. The wild-type protein and the mutant K96A cloned in pET28a vector were ordered from GenScript. The N-terminally truncated constructs were cloned by amplifying the sequence from the original vector and subcloning into BsaI-cleaved plasmid pNIC28_Bsa4 by SLiCE cloning (83). The construct pSLI-GSK3-GFP-glms was generated by PCR-amplification of 1013 bp of the C-terminal GSK3 coding sequence from genomic DNA using primers GSK3_NotI_sense_SLI and GSK3_AvrII_as_fored_int and cloning into pSLI-GFP-glms (84, 85) using NotI/AvrII restriction sites.

PfGSK3 expression and purification

E. coli C41(DE3) culture transformed with the PfGSK3 coding vector was grown in TB medium supplemented with 0.1 mg/ml ampicillin at 37°C, induced at OD_{600nm}=0.7 with 0.5 mM IPTG and harvested after 4 hours. The pellets were resuspended in 5 mL of lysis buffer (20mM NaP pH 7.5, 300mM NaCl, 15mM imidazole, 5% glycerol, 0.5mM TCEP, 1 mg/ml lysozyme, 5 U/ml DNase, 1 Roche protease inhibitor tablet/100mL) per 1 g of wet weight culture. The suspension was passed three times through an emulsifier at 15 000 psi, centrifuged at 19 000 x g and the supernatant was loaded on a pre-equilibrated His-Trap column. The column was washed with lysis buffer supplemented with 40 mM imidazole and the protein was eluted at increasing imidazole concentrations. The protein containing fractions were concentrated (10 kDa cut-off concentrator) with the addition of 1 mg of 3C protease per 3 L of

405 culture volume and further separated on a Superdex 200 HiLoad column (GE Healthcare) in
406 50mM Tris pH 8.0, 20mM NaCl, 0.5mM TCEP. The protein containing fractions were
407 concentrated again, loaded on ResourceQ anion exchange column (GE Healthcare) and
408 eluted with increasing concentration of NaCl. Fractions representing different PfGSK3 species
409 were pooled together, concentrated, dialyzed against the analysis buffer (typically 20mM Tris
410 pH 8.0, 100mM NaCl, 0.5mM TCEP) and flash-frozen in liquid nitrogen and stored at -80°C.
411 All purification steps were performed at 4°C.

412 **Expression and purification of insoluble PfGSK3 constructs**

413 The insoluble PfGSK3 constructs (K96A, S226A/Y229A, ΔN64) were expressed as described
414 for the wild-type PfGSK3. The pellets of harvested bacteria were resuspended in 5 mL of lysis
415 buffer (20mM NaP pH 7.5, 300mM NaCl, 15mM imidazole, 5% glycerol, 0.5mM TCEP, 1
416 mg/ml lysozyme, 5 U/ml DNase, 1 Roche protease inhibitor tablet/100mL) per 1 g of wet
417 weight culture. The suspension was passed three times through an emulsifier at 15 000 psi,
418 centrifuged at 19 000 x g and the pellet was dissolved in a denaturating buffer (20mM NaP
419 (pH 7.5), 300mM NaCl, 25mM imidazole, 5% glycerol, 6M urea, 0.5mM TCEP) and incubated
420 with 1 mL NiNTA bead slurry (Sigma) for 1h, 4°C. The beads were subsequently washed twice
421 with 10 ml of the same buffer and subsequently eluted with 5 ml of the same buffer containing
422 extra 250 mM imidazole. The protein was concentrated (10 kDa c/o) and the sample for mass
423 spectrometry was separated by SDS-PAGE gel.

424 **Small-scale expression tests**

425 4 mL of TB supplemented with ampicillin was inoculated wit pre-cultured *E. coli* C41(DE3) that
426 had been transformed with the tested plasmids. The cultures were grown at 37°C until the
427 OD_{600nm} =0.6 and further either induced with 0.5mM IPTG and grown for 4 hours at 37°C or
428 25°C, or induced with 0.1mM IPTG and grown for 16 h at 18°C. OD_{600nm} was measured and
429 culture volume corresponding to OD_{600nm} of 2.0/mL was harvested. The pellets were
430 resuspended in 400 µl of lysis buffer (lysate fractions), then lysed by 10 min of vortexing with

100 µl glass beads and the cell debris were removed by centrifugation (soluble fractions). 5 µl of each fraction was mixed with 10 µl of loading dye and run on SDS-PAGE in duplicates. One gel of each set of samples was blotted on PVDF membrane (*BioRad*) The membranes were blocked by 1% BSA in TBS-T, washed, incubated for 1h with a HisProbe-HRP conjugated antibody (ThermoFisher), washed with TBS-T and the blot was developed using Super Signal West Pico Substrate (ThermoFisher) and Super Signal West Femto Substrate (ThermoFisher) in a 1:10 ratio.

Glutaraldehyde cross-linking

1 mg/ml PfGSK3 in PBS and 0.5mM TCEP was mixed with 8x molar excess of either EDTA or $ZnCl_2$ and 0.01% glutaraldehyde. The reaction was quenched with 330mM Tris (final concentration) and SDS-PAGE loading dye and SDS-PAGE was run for 150 minutes at 150V. The gels were stained with Direct Blue stain.

Thermal shift assay

The stability of PfGSK3 under different buffer conditions and additives was measured by nanoDSF (Prometheus NT.48, NanoTemper Technologies, GmbH). The protein concentration was adjusted to 1 mg/ml. 10 µl of samples were loaded in the glass capillaries and heated from 20°C to 90°C with a heating rate of 1°C/min. The fluorescence signals with excitation wavelength of 280 nm and emission wavelengths of 330 and 350 nm were recorded and the melting temperature was calculated as maximum of the derivative of the fluorescence at 330 nm.

Circular dichroism

Circular dichroism was measured on a Chirascan CD spectrometer (Applied Photophysics). The protein concentration was adjusted to 1 µM by 2 mM NaP (pH 7.5), 4 mM NaCl, 0.05 mM TCEP prior to the measurement. The circular dichroism spectrum was measured 10x between 185 nm and 260 nm with 1 nm step in 1 mm quartz cuvette and analyzed by the CDSSTR algorithm (86, 87) using DichroWeb (88).

457 **Analytical size exclusion chromatography**

458 The analytical size exclusion chromatography was performed on an Agilent Bio-LC system
459 using a home-packed Superose 5/150 column (25 µl sample) or a Superose 6 Increase 10/300
460 column (100 µl sample). PBS supplemented with 0.5mM TCEP was used as a mobile phase
461 and the resulting chromatograms were recorded using the as fluorescence signal with
462 excitation wavelength of 280 nm and emission wavelength of 350 nm as readout.

463 **Autophosphorylation IEX assay**

464 0.5 mg/ml of PfGSK3 was incubated at 37°C with 2mM ATP or cAMP and 10mM $MgCl_2$
465 overnight. The samples were subsequently dialyzed at 4°C overnight in 50mM Tris pH 8.0,
466 20mM NaCl, 0.5mM TCEP. The samples were analyzed by analytical ion exchange
467 chromatography using a Resource Q column (GE Healthcare) and the 1260 Infinity Bio-inert
468 high-performance liquid chromatography system (Agilent Technologies) at 10 °C. The system
469 and column were equilibrated in 50mM Tris pH 8.0, 20mM NaCl, 0.5mM TCEP. 100 µl of
470 sample was injected and eluted with an increasing concentration of NaCl. The system was
471 run at 0.2 ml/min ad the elution profile was analyzed by UV fluorescence detector with
472 absorbance at 280 nm and emission at 350 nm.

473 **Small angle X-ray scattering**

474 The SAXS data were collected at the P12 BioSAXS Beamline at the PETRA III storage ring
475 (c/o DESY, Hamburg, Germany) (89). The concentrated samples were dialyzed against
476 (20 mM Tris pH 8.0, 100 mM NaCl, 0.5 mM TCEP overnight at 4°C and the concentration was
477 adjusted to 10 mg/ml The X-ray scattering data were measured in an on-line SEC-SAXS
478 mode, using a SD200 Increase 5/150 column (GE Healthcare) at 0.4 ml/min with 1 frame
479 recorded per second (Table 1). The data were automatically processed using the SASFLOW
480 pipeline (90) and further analyzed using the ATSAS suite (91) of programs to determine the
481 molar mass, radius of gyration and real-space distance distribution. Scattering curves were
482 computed from models using CRYSOL (92) with a constant subtraction and maximum order
483 of harmonics set to 50. The rigid body modelling performed using CORAL (71), setting different

parts of models yielding best CRYSOL fits as disordered. These were residues 1-65 and 403-440 in conformation A, resides 47-65 and 403-440 in conformation B and residues 403-440 in conformation C. The raw data were uploaded to SASBDB under accession numbers SASDL77 and SASDL87.

Kinase assay

To investigate enzymatic activity of recombinant PfGSK3 a commercial luminescence-based kinase assay (KinaseGlo Plus, Promega) was used as previously described (93). Briefly, 20 ng PfGSK3, 12 µM GS-1 peptide substrate (residues 636-661 of the human glycogen synthase 1; sequence YRRAAVPPSPSLSRHSSPHQ(pS)EDEEE; pS = prephosphorylated serine, Promega) and 6 µM ATP (UltraPure, Promega) in the kinase reaction buffer (40 mM Tris-HCl pH 7.5; 20 mM $MgCl_2$; 0.1 mg/mL BSA) were used as standard reaction mix (final reaction volume 5 µl). The kinase reaction was performed for 30 min at 30°C followed by incubation with KinaseGlo reagent according to the manufacturer's instructions. The reaction was transferred to a solid white 384-well plate (NUNC, ThermoFisher) and the luminescence signal was measured in an EnVision Multilabel Plate Reader (PerkinElmer, Integration time 0.5 sec/well). To investigate reaction kinetics, kinase and substrate concentrations were varied between 0 and 100 ng or 0 and 15 µM respectively. To investigate autophosphorylation, reactions were performed with kinase concentrations between 0 and 500 ng, 30 µM ATP and without a substrate.

***P. falciparum* culture**

Parasites were cultured in 5% 0^+ human erythrocytes (Blood bank, Universitätklinikum Hamburg Eppendorf) in RPMI medium supplemented with 0.5% Albumax at 37°C in an atmosphere of 1% O_2, 5% CO_2 and 94% N_2 as described previously (94). Parasitemia was monitored by Giemsa-staining of methanol-fixed blood smears. The parasite strain 3D7 was used in this study (95).

Parasite imaging

For live cell imaging parasite cultures were pelleted by centrifugation at 500x g for 1 min. Sedimented cells were resuspended in an equal volume of the supernatant, 5 µl of the sample were placed on a microscopy slide and covered with a cover slip. Fluorescence microscopy images were taken with a Leica DM6 B microscope equipped with Leica DFC9000 GT camera using an 100x immersion oil objective. Images were aquired with Leica Application Suite X (LAS X) software and processed using Adobe Photoshop CS2. Nuclei were stained with 1 µg/ml DAPI (Biomol) in RPMI at 37°C for 15 min.

Generation of transgenic parasite lines

For Transfection, mature schizonts were enriched using 60% percoll and electroporated with 50 µg of plasmid DNA using a Lonza Nucleofector II (96). Transfectants were seleceted with 4nM WR99210 (Jacobus Pharmaceuticals). Stable integrant cell lines were generated as previously described (84). Briefly, parasites carrying the WR99210-selected episomal plasmid were cultivated in the presence of 400 µg/ml G418 (Sigma) to select for integrants with the desired modification of the genomic locus. Correct genomic integration of the construct was confirmed by PCR using genomic DNA from G418-selected integrants and 3D7 wildtype. Genomic DNA was isolated using QIAamp DNA Mini Kit. For PCR analysis primers specific for 3' and 5' integration as well as wildtype locus of PfGSK3 were used.

Purification of GSK3-GFP from *P. falciparum*

For purification of GSK3-GFP, parasites were synchronized by treatment with 5% sorbitol for 10 min at 37°C and subsequently cultured in a volume of 50 ml with 5% hematocrit. Culture medium was changed daily until parasitemia had reached 8-10%. Erythrocytes were lysed with 0.03% saponin, isolated parasites were washed three times with ice cold PBS and resuspended in 2 ml lysis buffer (50 mM Tris-HCl pH 7.5, 150 mM NaCl, 0.5 mM TCEP, 1x protease inhibitor mix, 50 U/mL DNase). The sample was triturated five times through a 27G-needle (Braun) and further lysed by three cycles of freezing at -80°C followed by thawing on ice. The lysates were supplemented with 1% DDM and 0.1% CHS and incubated for 3 hours

at 4°C. Subsequently, the samples were mixed with 30 µl of GFP-Trap bead slurry (ChromoTek) and incubated on a rotatory wheel for 3 hours at 4°C. The beads were then washed with 1 ml of 150 mM NaCl, 10 mM Tris, protease inhibitor mix (Roche), 0.1% DDM, 0.01% CHS pH 7.5 and with 1 ml of 300 mM NaCl, 10 mM Tris, protease inhibitor mix, 0.02% DDM, 0.002% CHS pH 7.5. The trapped proteins were eluted with 30 µl of 6% SDS, 250 mM Tris-HCl, pH 6.8, 71 mM TCEP at 95°C.

Sample preparation for mass spectrometry

In-solution samples from parasite cell cultures were processed as previously described (97). To assess the phosphorylation status of the recombinant PfGSK3 (purified protein, separated IEX fractions, insoluble constructs), each sample was separated on SDS-PAGE gel. Coomassie-stained bands were excised, chopped into small pieces and transferred to 0.5 ml Eppendorf tubes. For all following steps, buffers were exchanged by two consecutive 15 min incubation steps of the gel pieces with 200 µl of acetonitrile (ACN), whereby the ACN was removed after each step. Proteins were reduced by the addition of 200 µl of a 10 mM DTT solution in 100 mM ammonium bicarbonate (AmBiC, Sigma Aldrich, A6141) and incubation at 56°C for 30 min. Proteins were alkylated by the addition of 200 µl of 55 mM chloroacetamide (CAA)100 mM AmBiC solution and incubation for 20 min in the dark. A 0.1 µg/µl stock solution of trypsin (Promega, V511A) in trypsin resuspension buffer (Promega, V542A) was diluted with ice-cold 50 mM AmBiC buffer to achieve a final concentration of 1 ng/µl. 50 µl thereof were added to gel pieces, which were incubated first for 30 min on ice and then over night at 37°C. Gel pieces were sonicated for 15 min, spun down and the supernatant was transferred into a glass vial (VDS Optilab, 93908556). Remaining gel pieces were washed with 50 µl of an aqueous solution of 50% ACN and 1% formic acid and sonicated for 15 min. The combined supernatants were dried in a speedvac and reconstituted in 10 µl of an aqueous solution of 0.1% (v/v) formic acid.

Mass spectrometry data acquisition

562 The mass spectra of the initial phosphorylation site assessment of PfGSK3 (Fig. SB) was
563 performed as follows: An UltiMate 3000 RSLC nano LC system (Dionex) fitted with a trapping
564 cartridge (Precolumn C18 PepMap100, 5 mm, 300 µm i.d., 5 µm, 100 Å) and an analytical
565 column (Acclaim PepMap 100. 75 × 50 cm C18, 3 mm, 100 Å) was used. Trapping was carried
566 out with a constant flow of trapping solution (0.05% trifluoroacetic acid in water) at 30 µL/min
567 onto the trapping column for 6 minutes. Subsequently, peptides were eluted via the analytical
568 column running solvent A (0.1% formic acid in water) with a constant flow of 0.3 µL/min, with
569 increasing percentage of solvent B (0.1% formic acid in acetonitrile) from 2% to 4% in 4 min,
570 from 4% to 8% in 2 min, then 8% to 28% for a further 37 min, in another 9 min. from 28%-
571 40%, and finally 40%-80% for 3 min followed by re-equilibration back to 2% B in 5 min. The
572 outlet of the analytical column was coupled directly to an Orbitrap QExactive™ plus Mass
573 Spectrometer (Thermo) using the Nanospray Flex™ ion source in positive ion mode. The
574 QExactive plus was operated in positive ion mode with a spray voltage of 2.2 kV and capillary
575 temperature of 275°C. Full scan MS spectra with a mass range of 350–1400 m/z were
576 acquired in profile mode using a resolution of 70,000 (maximum injections time of 100 ms,
577 AGC target was set to $3x10^6$ ions). Precursors were isolated using the quadrupole with a
578 window of 1.7 m/z and fragmentation was triggered by HCD in fixed collision energy mode
579 with fixed collision energy of 28%. MS2 spectra were acquired with the Orbitrap with a
580 resolution of 17.500 and a max injection time of 70 ms.

581 The mass spectra of all other experiments were recorded as follows: Peptides were analyzed
582 by LC-MS/MS on an Orbitrap Fusion Lumos mass spectrometer (Thermo Scentific) as
583 previously described (98). To this end, peptides were separated using an Ultimate 3000 nano
584 RSLC system (Dionex) equipped with a trapping cartridge (Precolumn C18 PepMap100, 5
585 mm, 300 µm i.d., 5 µm, 100 Å) and an analytical column (Acclaim PepMap 100. 75 × 50 cm
586 C18, 3 mm, 100 Å) connected to a nanospray-Flex ion source. For the detection of
587 posttranslational modified peptides, peptides were loaded onto the trap column at 30 µl per
588 min using solvent A (0.1% formic acid) and peptides were eluted using a gradient from 2 to

589 80% Solvent B (0.1% formic acid in acetonitrile) over 60 min at 0.3 µl per min (all solvents
590 were of LC-MS grade). The Orbitrap Fusion Lumos was operated in positive ion mode with a
591 spray voltage of 2.4 kV and capillary temperature of 275 °C. Full scan MS spectra with a mass
592 range of 375–1200 m/z were acquired in profile mode using a resolution of 120,000 (maximum
593 injections time of 50 ms, AGC target was set to Standard with a max injection time of 50 ms.
594 Precursors were isolated using the quadrupole with a window of 1.2 m/z and fragmentation
595 was triggered by HCD in fixed collision energy mode with fixed collision energy of 34%. MS2
596 spectra were acquired with the Orbitrap with a resolution of 15.000 and a max injection time
597 of 54 ms.

598 **Mass spectrometry data analysis**

599 Acquired data were analyzed using IsobarQuant (99) and Mascot V2.4 (Matrix Science) using
600 a reverse UniProt FASTA database from *E. coli* (UP000000625) or *Plasmodium falciparum*
601 (UP000001450) including common contaminants. The following modifications were taken into
602 account: Carbamidomethyl (C, fixed), Acetyl (K, variable), Acetyl (Protein N-term, variable),
603 Oxidation (M, variable), as well as the variable modification Phospho (ST) and Phospho (Y).
604 The mass error tolerance for full scan MS spectra was set to 10 ppm and to 0.02 Da for MS/MS
605 spectra. A maximum of 2 missed cleavages were allowed. A minimum of 2 unique peptides
606 with a peptide length of at least seven amino acids and a false discovery rate below 0.01 were
607 required on the peptide and protein level (100). Prior performing the search, the protein
608 sequences corresponding to the expressed PfGSK3 constructs were added to the database
609 for the expression host. The raw data have been uploaded to the PRIDE database with the
610 dataset identifier PXD026387.

611 **Correlation analysis**

612 Each biological replicate of mass spectrometry experiment was paired with the corresponding
613 biological replicate of the activity measurement. The relative phosphorylation of a residue was
614 calculated as a ratio of number of time the residue was identified as phosphorylated (Mascot

score >32 and MD score >=5) to number of times the residue was identified in the biological sample. The relative activity was calculated as buffer-subtracted readout of the luciferase assay relative to control. The strength of the linear association was calculated as Pearson correlation coefficient using R (101).

Negative stain electron microscopy

4 µl of 0.01 mg/ml protein solution was applied to carbon-coated Cu/Pd grids and incubated for 1 min. Excess liquid was removed with the filter paper (Whatman), and the grid was washed twice with water for 5 s and 30 s. 4 µl of 2% uranyl acetate were applied twice for 5 s and 30 s. The micrographs were collected on a Talos L120C (CSSB Cryo-EM multiuser facility) with 70 000x magnification.

Bioinformatics

The homologous protein sequences were aligned with the program MAFFT (102) and depicted in Jalview. The secondary structure was predicted by Jpred (103). The PfGSK3 structures were predicted using the Robetta server and the TrRefineRosetta method (70). To simulate the different N-terminally phosphorylated species present in the protein fractions, we generated five models for each of the following PfGSK3 sequences: wild-type sequence, three sequences with a single phosphomimetic mutation (S40E, S42E, S43E) and one with a triple mutation S40E/S42E/S43E (abbreviated SE3). Per-residue local error estimates of the models calculated by Robetta (104) are written in the B-factor column of the PDB files. For phylogenetic analysis, protein sequences with highest identity scores were identified for individual organisms with the blastp suite of NCBI (105), the sequences were aligned with the ClustalW method and the R package msa (106), and the phylogenetic tree was calculated in PhyML with LG +G+I+F method (107). The phylogenetic tree with multiple sequence alignment was plotted using R package ggtree (108).

Data availability

The mass spectrometry data are available in PRIDE database with dataset identifier PXD026387. The SAXS data have been deposited in the SASBDB, accession numbers SASDL77 and SASDL87. All other raw data are available on Figshare (doi: 10.6084/m9.figshare.14806887).

Supporting information

This article contains supporting information.

Acknowledgments

We thank the Sample Preparation and Characterization facility of EMBL Hamburg for support in nanoDSF, CD and DLS measurements. We also thank the Proteomics Core Facility of EMBL for the support in mass spectrometry sample preparation, measurements and analysis. We thank Maxime Killer and Vadim Kotov for the help with EM data acquisition and processing. Part of this work was performed at the CryoEM Facility at CSSB, supported by the UHH and DFG grant numbers (INST 152/772-1|152/774-1|152/775-1|152/776-1|152/777-1 FUGG). This work was supported by a grant from the Joachim Herz foundation (Nr. 800026) and the BMBF (grant number: 05K18YEA). AA is grateful for support by a Jürgen Manchot Stiftung fellowship.

Conflict of interests

The authors declare that they have no conflicts of interest with the contents of this article.

References

1. World Health Organization (2019) *World Malaria Report. https://www.who.int/malaria*
2. Haldar, K., Bhattacharjee, S., and Safeukui, I. (2018) Drug resistance in Plasmodium. *Nat. Rev. Microbiol.* **16**, 156–170
3. Santos, R., Ursu, O., Gaulton, A., Bento, A. P., Donadi, R. S., Bologa, G., Karlsson, A., Al-lazikani, B., Hersey, A., Oprea, T. I., and Overington, J. P. (2017) A comprehensive map of molecular drug targets. *Nat. Rev. Drug Discov.* **16**, 19–34
4. Cabrera, D. G., Horatscheck, A., Wilson, C. R., Basarab, G., Eyermann, C. J., and Chibale, K. (2018) Plasmodial Kinase Inhibitors: License to Cure? *J. Med. Chem.* **61**, 8061–8077
5. PARKER, P. J., CAUDWELL, F. B., and COHEN, P. (1983) Glycogen Synthase from Rabbit Skeletal Muscle; Effect of Insulin on the State of phosphorylation of the Seven Phosphoserine Residues in vivo. *Eur. J. Biochem.* 10.1111/j.1432-1033.1983.tb07140.x
6. Cross, D. A. E., Alessi, D. R., Cohen, P., Andjelkovich, M., and Hemmings, B. A. (1995) Inhibition of glycogen synthase kinase-3 by insulin mediated by protein kinase B. *Nature*. 10.1038/378785a0
7. Welsh, G. I., and Proud, C. G. (1993) Glycogen synthase kinase-3 is rapidly inactivated in response to insulin and phosphorylates eukaryotic initiation factor eIF-2B. *Biochem. J.* 10.1042/bj2940625
8. Diehl, J. A., Cheng, M., Roussel, M. F., and Sherr, C. J. (1998) Glycogen synthase kinase-3β regulates cyclin D1 proteolysis and subcellular localization. *Genes Dev.* 10.1101/gad.12.22.3499
9. Yamamoto, H., Kishida, S., Kishida, M., Ikeda, S., Takada, S., and Kikuchi, A. (1999) Phosphorylation of axin, a Wnt signal negative regulator, by glycogen synthase kinase-3β regulates its stability. *J. Biol. Chem.* 10.1074/jbc.274.16.10681
10. Turenne, G. A., and Price, B. D. (2001) Glycogen synthase kinase3 beta phosphorylates serine 33 of p53 and activates p53's transcriptional activity. *BMC Cell Biol.* 10.1186/1471-2121-2-12
11. Ikeda, S., Kishida, S., Yamamoto, H., Murai, H., Koyama, S., and Kikuchi, A. (1998) Axin, a negative regulator of the Wnt signaling pathway, forms a complex with GSK-3β and β-catenin and promotes GSK-3β-dependent phosphorylation of β-catenin. *EMBO J.* 10.1093/emboj/17.5.1371
12. Hanger, D. P., Hughes, K., Woodgett, J. R., Brion, J. P., and Anderton, B. H. (1992) Glycogen synthase kinase-3 induces Alzheimer's disease-like phosphorylation of tau: Generation of paired helical filament epitopes and neuronal localisation of the kinase. *Neurosci. Lett.* 10.1016/0304-3940(92)90774-2
13. Yang, S. - D, Song, J. - S, Yu, J. - S, and Shiah, S. - G (1993) Protein Kinase FA/GSK- 3 Phosphorylates on Ser235- Pro and Ser404- Pro that Are Abnormally Phosphorylated in Alzheimer's Disease Brain. *J. Neurochem.* 10.1111/j.1471-4159.1993.tb09811.x
14. Aplin, A. E., Gibb, G. M., Jacobsen, J. S., Gallo, J. M., and Anderton, B. H. (1996) In vitro phosphorylation of the cytoplasmic domain of the amyloid precursor protein by glycogen synthase kinase-3β. *J. Neurochem.* 10.1046/j.1471-4159.1996.67020699.x
15. Ryder, J., Su, Y., Liu, F., Li, B., Zhou, Y., and Ni, B. (2003) Divergent roles of GSK3 and CDK5 in APP processing. *Biochem. Biophys. Res. Commun.* 10.1016/j.bbrc.2003.11.014
16. Ferrao Santos, S., Tasiaux, B., Sindic, C., and Octave, J. N. (2011) Inhibition of neuronal calcium oscillations by cell surface APP phosphorylated on T668. *Neurobiol. Aging*. 10.1016/j.neurobiolaging.2010.01.006
17. Eldar-Finkelman, H., and Martinez, A. (2011) GSK-3 Inhibitors: Preclinical and Clinical

Focus on CNS. *Front. Mol. Neurosci.* **4**, 1–18

18. Bourel, E., Grieco, S. F., and Jope, R. S. (2016) Glycogen synthase kinase-3 (GSK3): regulation, actions, and diseases. 10.1016/j.pharmthera.2014.11.016.Glycogen

19. Jope, R. S. (2011) Glycogen Synthase Kinase-3 in the Etiology and Treatment of Mood Disorders. *Front. Mol. Neurosci.* 10.3389/fnmol.2011.00016

20. Singh, K. K. (2013) An emerging role for Wnt and GSK3 signaling pathways in schizophrenia. *Clin. Genet.* 10.1111/cge.12111

21. De Sarno, P., Axtell, R. C., Raman, C., Roth, K. A., Alessi, D. R., and Jope, R. S. (2008) Lithium Prevents and Ameliorates Experimental Autoimmune Encephalomyelitis. *J. Immunol.* 10.4049/jimmunol.181.1.338

22. Del Ser, T., Steinwachs, K. C., Gertz, H. J., Andrés, M. V., Gómez-Carrillo, B., Medina, M., Vericat, J. A., Redondo, P., Fleet, D., and León, T. (2013) Treatment of Alzheimer's disease with the GSK-3 inhibitor tideglusib: A pilot study. *J. Alzheimer's Dis.* 10.3233/JAD-2012-120805

23. Lovestone, S., Boada, M., Dubois, B., Hüll, M., Rinne, J. O., Huppertz, H. J., Calero, M., Andrés, M. V., Gómez-Carrillo, B., León, T., and Del Ser, T. (2015) A phase II trial of tideglusib in alzheimer's disease. *J. Alzheimer's Dis.* 10.3233/JAD-141959

24. Ter Haar, E., Coll, J. T., Austen, D. A., Hsiao, H. M., Swenson, L., and Jain, J. (2001) Structure of GSK3β reveals a primed phosphorylation mechanism. *Nat. Struct. Biol.* **8**, 593–596

25. Dajani, R., Fraser, E., Roe, S. M., Young, N., Good, V., Dale, T. C., and Pearl, L. H. (2001) Crystal structure of glycogen synthase kinase 3β: Structural basis for phosphate-primed substrate specificity and autoinhibition. *Cell*. **105**, 721–732

26. Hughes, K., Nikolakaki, E., Plyte, S. E., Totty, N. F., and Woodgett, J. R. (1993) Modulation of the glycogen synthase kinase-3 family by tyrosine phosphorylation. *EMBO J.* 10.1002/j.1460-2075.1993.tb05715.x

27. Lochhead, P. A., Kinstrie, R., Sibbet, G., Rawjee, T., Morrice, N., and Cleghon, V. (2006) A chaperone-dependent GSK3β transitional intermediate mediates activation-loop autophosphorylation. *Mol. Cell*. **24**, 627–633

28. Cole, A. R., Causeret, F., Yadirgi, G., Hastie, C. J., McLauchlan, H., McManus, E. J., Hernández, F., Eickholt, B. J., Nikolic, M., and Sutherland, C. (2006) Distinct priming kinases contribute to differential regulation of collapsin response mediator proteins by glycogen synthase kinase-3 in vivo. *J. Biol. Chem.* 10.1074/jbc.M513344200

29. Cole, A. R., Knebel, A., Morrice, N. A., Robertson, L. A., Irving, A. J., Connolly, C. N., and Sutherland, C. (2004) GSK-3 phosphorylation of the Alzheimer epitope within collapsin response mediator proteins regulates axon elongation in primary neurons. *J. Biol. Chem.* 10.1074/jbc.C400412200

30. Sutherland, C., Leighton, I. A., and Cohen, P. (1993) Inactivation of glycogen synthase kinase-3β by phosphorylation: New kinase connections in insulin and growth-factor signalling. *Biochem. J.* **2296**, 15–19

31. Wichers, J. S., Scholz, J. A. M., Strauss, J., Witt, S., Lill, A., Ehnold, L. I., Neupert, N., Liffner, B., Lühken, R., Petter, M., Lorenzen, S., Wilson, D. W., Löw, C., Lavazec, C., Bruchhaus, I., Tannich, E., Gilberger, T. W., and Bachmann, A. (2019) Dissecting the gene expression, localization, membrane topology, and function of the plasmodium falciparum STEVOR protein family. *MBio*. 10.1128/mBio.01500-19

32. Prinz, B., Harvey, K. L., Wilcke, L., Ruch, U., Engelberg, K., Biller, L., Lucet, I., Erkelenz, S., Heincke, D., Spielmann, T., Doerig, C., Kunick, C., Crabb, B. S., Gilson, P. R., and Gilberger, T. W. (2016) Hierarchical phosphorylation of apical membrane antigen 1 is required for efficient red blood cell invasion by malaria parasites. *Sci. Rep.* **6**, 34479

33. Mordue, D. G., Desai, N., Dustin, M., and Sibley, L. D. (1999) Invasion by Toxoplasma gondii establishes a moving junction that selectively excludes host cell plasma membrane proteins on the basis of their membrane anchoring. *J. Exp. Med.*

10.1084/jem.190.12.1783

34. Narum, D. L., and Thomas, A. W. (1994) Differential localization of full-length and processed forms of PF83/AMA-1 an apical membrane antigen of Plasmodium falciparum merozoites. *Mol. Biochem. Parasitol.* 10.1016/0166-6851(94)90096-5

35. Triglia, T., Healer, J., Caruana, S. R., Hodder, A. N., Anders, R. F., Crabb, B. S., and Cowman, A. F. (2000) Apical membrane antigen 1 plays a central role in erythrocyte invasion by Plasmodium species. *Mol. Microbiol.* 10.1046/j.1365-2958.2000.02175.x

36. Treeck, M., Zacherl, S., Herrmann, S., Cabrera, A., Kono, M., Struck, N. S., Engelberg, K., Haase, S., Frischknecht, F., Miura, K., Spielmann, T., and Gilberger, T. W. (2009) Functional analysis of the leading malaria vaccine candidate AMA-1 reveals an essential role for the cytoplasmic domain in the invasion process. *PLoS Pathog.* 10.1371/journal.ppat.1000322

37. Treeck, M., Sanders, J. L., Elias, J. E., and Boothroyd, J. C. (2011) The phosphoproteomes of plasmodium falciparum and toxoplasma gondii reveal unusual adaptations within and beyond the parasites' boundaries. *Cell Host Microbe*. **10**, 410–419

38. Solyakov, L., Halbert, J., Alam, M. M., Semblat, J.-P., Dorin-Semblat, D., Reininger, L., Bottrill, A. R., Mistry, S., Abdi, A., Fennell, C., Holland, Z., Demarta, C., Bouza, Y., Sicard, A., Nivez, M.-P., Eschenlauer, S., Lama, T., Thomas, D. C., Sharma, P., Agarwal, S., Kern, S., Pradel, G., Graciotti, M., Tobin, A. B., and Doerig, C. (2011) Global kinomic and phospho-proteomic analyses of the human malaria parasite Plasmodium falciparum. *Nat. Commun.* **2**, 565

39. Lasonder, E., Green, J. L., Camarda, G., Talabani, H., Holder, A. A., Langsley, G., and Alano, P. (2012) The plasmodium falciparum schizont phosphoproteome reveals extensive phosphatidylinositol and cAMP-protein kinase A signaling. *J. Proteome Res.* **11**, 5323–5337

40. Vulliez-Le Normand, B., Tonkin, M. L., Lamarque, M. H., Langer, S., Hoos, S., Roques, M., Saul, F. A., Faber, B. W., Bentley, G. A., Boulanger, M. J., and Lebrun, M. (2012) Structural and functional insights into the malaria parasite moving junction complex. *PLoS Pathog.* 10.1371/journal.ppat.1002755

41. Cao, J., Kaneko, O., Thongkukiatkul, A., Tachibana, M., Otsuki, H., Gao, Q., Tsuboi, T., and Torii, M. (2009) Rhoptry neck protein RON2 forms a complex with microneme protein AMA1 in Plasmodium falciparum merozoites. *Parasitol. Int.* 10.1016/j.parint.2008.09.005

42. Besteiro, S., Michelin, A., Poncet, J., Dubremetz, J. F., and Lebrun, M. (2009) Export of a Toxoplasma gondii rhoptry neck protein complex at the host cell membrane to form the moving junction during invasion. *PLoS Pathog.* 10.1371/journal.ppat.1000309

43. Alexander, D. L., Mital, J., Ward, G. E., Bradley, P., and Boothroyd, J. C. (2005) Identification of the moving junction complex of Toxoplasma gondii: A collaboration between distinct secretory organelles. *PLoS Pathog.* 10.1371/journal.ppat.0010017

44. Alexander, D. L., Arastu-Kapur, S., Dubremetz, J. F., and Boothroyd, J. C. (2006) Plasmodium falciparum AMA1 binds a rhoptry neck protein homologous to TgRON4, a component of the moving junction in Toxoplasma gondii. *Eukaryot. Cell*. 10.1128/EC.00040-06

45. Leykauf, K., Treeck, M., Gilson, P. R., Nebl, T., Braulke, T., Cowman, A. F., Gilberger, T. W., and Crabb, B. S. (2010) Protein kinase a dependent phosphorylation of apical membrane antigen 1 plays an important role in erythrocyte invasion by the malaria parasite. *PLoS Pathog.* 10.1371/journal.ppat.1000941

46. Hodder, A. N., Crewther, P. E., Matthewll, M. L. S. M., Reid, G. E., Moritz, R. L., Simpson, R. J., and Anders, R. F. (1996) The disulfide bond structure of Plasmodium apical membrane antigen-1. *J. Biol. Chem.* 10.1074/jbc.271.46.29446

47. Patel, A., Perrin, A. J., Flynn, H. R., Bisson, C., Withers-Martinez, C., Treeck, M.,

Flueck, C., Nicastro, G., Martin, S. R., Ramos, A., Gilberger, T. W., Snijders, A. P., Blackman, M. J., and Baker, D. A. (2019) Cyclic AMP signalling controls key components of malaria parasite host cell invasion machinery. *PLoS Biol.* 10.1371/journal.pbio.3000264

48. Wilde, M. L., Triglia, T., Marapana, D., Thompson, J. K., Kouzmitchev, A. A., Bullen, H. E., Gilson, P. R., Cowman, A. F., and Tonkina, C. J. (2019) Protein kinase A is essential for invasion of Plasmodium falciparum into human erythrocytes. *MBio*. **10**, 1–15

49. Fugel, W., Oberholzer, A. E., Gschloessl, B., Dzikowski, R., Pressburger, N., Preu, L., Pearl, L. H., Baratte, B., Ratin, M., Okun, I., Doerig, C., Kruggel, S., Lemcke, T., Meijer, L., and Kunick, C. (2013) 3,6-Diamino-4-(2-halophenyl)-2-benzoylthieno[2,3-b]pyridine-5-carbonitriles are selective inhibitors of Plasmodium falciparum glycogen synthase kinase-3. *J Med Chem*. **56**, 264–275

50. Masch, A., Nasereddin, A., Alder, A., Bird, M. J., Schweda, S. I., Preu, L., Doerig, C., Dzikowski, R., Gilberger, T. W., and Kunick, C. (2019) Structure-activity relationships in a series of antiplasmodial thieno[2,3-b]pyridines. *Malar. J.* **18**, 1–10

51. Moolman, C., van der Sluis, R., Beteck, R. M., and Legoabe, L. J. (2021) Exploration of benzofuran-based compounds as potent and selective Plasmodium falciparum glycogen synthase kinase-3 (PfGSK-3) inhibitors. *Bioorg. Chem.* **112**, 104839

52. OSOLODKIN, D. I., ZAKHAREVICH, N. V., PALYULIN, V. A., DANILENKO, V. N., and ZEFIROV, N. S. (2011) Bioinformatic analysis of glycogen synthase kinase 3: human versus parasite kinases. *Parasitology*. **138**, 725–735

53. Droucheau, E., Primot, A., Thomas, V., Mattei, D., Knockaert, M., Richardson, C., Sallicandro, P., Alano, P., Jafarshad, A., Baratte, B., Kunick, C., Parzy, D., Pearl, L., Doerig, C., and Meijer, L. (2004) Plasmodium falciparum glycogen synthase kinase-3: Molecular model, expression, intracellular localisation and selective inhibitors. *Biochim. Biophys. Acta - Proteins Proteomics*. **1697**, 181–196

54. Dajani, R., Fraser, E., Roe, S. M., Yeo, M., Good, V. M., Thompson, V., Dale, T. C., and Pearl, L. H. (2003) Structural basis for recruitment of glycogen synthase kinase 3β to the axin-APC scaffold complex. *EMBO J.* 10.1093/emboj/cdg068

55. Henley, Z. A., Bax, B. D., Inglesby, L. M., Champigny, A., Gaines, S., Faulder, P., Le, J., Thomas, D. A., Washio, Y., and Baldwin, I. R. (2017) From PIM1 to PI3Kδ via GSK3β: Target Hopping through the Kinome. *ACS Med. Chem. Lett.* 10.1021/acsmedchemlett.7b00296

56. Gentile, G., Merlo, G., Pozzan, A., Bernasconi, G., Bax, B., Bamborough, P., Bridges, A., Carter, P., Neu, M., Yao, G., Brough, C., Cutler, G., Coffin, A., and Belyanskaya, S. (2012) 5-Aryl-4-carboxamide-1,3-oxazoles: Potent and selective GSK-3 inhibitors. *Bioorganic Med. Chem. Lett.* 10.1016/j.bmcl.2012.01.034

57. Gentile, G., Bernasconi, G., Pozzan, A., Merlo, G., Marzorati, P., Bamborough, P., Bax, B., Bridges, A., Brough, C., Carter, P., Cutler, G., Neu, M., and Takada, M. (2011) Identification of 2-(4-pyridyl)thienopyridinones as GSK-3β inhibitors. *Bioorganic Med. Chem. Lett.* 10.1016/j.bmcl.2011.06.050

58. Chu, N., Salguero, A. L., Liu, A. Z., Chen, Z., Dempsey, D. R., Ficarro, S. B., Alexander, W. M., Marto, J. A., Li, Y., Amzel, L. M., Gabelli, S. B., and Cole, P. A. (2018) Akt Kinase Activation Mechanisms Revealed Using Protein Semisynthesis. *Cell*. 10.1016/j.cell.2018.07.003

59. Bax, B., Carter, P. S., Lewis, C., Guy, A. R., Bridges, A., Tanner, R., Pettman, G., Mannix, C., Culbert, A. A., Brown, M. J. B., Smith, D. G., and Reith, A. D. (2001) The structure of phosphorylated GSK-3β complexed with a peptide, FRATtide, that inhibits β-catenin phosphorylation. *Structure*. 10.1016/S0969-2126(01)00679-7

60. Liang, S. H., Chen, J. M., Normandin, M. D., Chang, J. S., Chang, G. C., Taylor, C. K., Trapa, P., Plummer, M. S., Para, K. S., Conn, E. L., Lopresti-Morrow, L., Lanyon, L. F., Cook, J. M., Richter, K. E. G., Nolan, C. E., Schachter, J. B., Janat, F., Che, Y., Shanmugasundaram, V., Lefker, B. A., Enerson, B. E., Livni, E., Wang, L., Guehl, N.

J., Patnaik, D., Wagner, F. F., Perlis, R., Holson, E. B., Haggarty, S. J., El Fakhri, G., Kurumbail, R. G., and Vasdev, N. (2016) Discovery of a Highly Selective Glycogen Synthase Kinase-3 Inhibitor (PF-04802367) That Modulates Tau Phosphorylation in the Brain: Translation for PET Neuroimaging. *Angew. Chemie - Int. Ed.* 10.1002/anie.201603797

61. Wang, Y., Wach, J. Y., Sheehan, P., Zhong, C., Zhan, C., Harris, R., Almo, S. C., Bishop, J., Haggarty, S. J., Ramek, A., Berry, K. N., O'Herin, C., Koehler, A. N., Hung, A. W., and Young, D. W. (2016) Diversity-Oriented Synthesis as a Strategy for Fragment Evolution against GSK3β. *ACS Med. Chem. Lett.* 10.1021/acsmedchemlett.6b00230

62. Pease, B. N., Huttlin, E. L., Jedrychowski, M. P., Talevich, E., Harmon, J., Dillman, T., Kannan, N., Doerig, C., Chakrabarti, R., Gygi, S. P., and Chakrabarti, D. (2013) Global analysis of protein expression and phosphorylation of three stages of *Plasmodium falciparum* intraerythrocytic development. *J. Proteome Res.* **12**, 4028–4045

63. Ganter, M., Goldberg, J. M., Dvorin, J. D., Paulo, J. A., King, J. G., Tripathi, A. K., Paul, A. S., Yang, J., Coppens, I., Jiang, R. H. Y., Elsworth, B., Baker, D. A., Dinglasan, R. R., Gygi, S. P., and Duraisingh, M. T. (2017) Plasmodium falciparum CRK4 directs continuous rounds of DNA replication during schizogony. *Nat. Microbiol.* **2**, 17017

64. Kumar, S., Kumar, M., Ekka, R., Dvorin, J. D., Paul, A. S., Madugundu, A. K., Gilberger, T., Gowda, H., Duraisingh, M. T., Keshava Prasad, T. S., and Sharma, P. (2017) PfCDPK1 mediated signaling in erythrocytic stages of Plasmodium falciparum. *Nat. Commun.* **8**, 1–12

65. Flueck, C., Drought, L. G., Jones, A., Patel, A., Perrin, A. J., Walker, E. M., Nofal, S. D., Snijders, A. P., Blackman, M. J., and Baker, D. A. (2019) Phosphodiesterase beta is the master regulator of camp signalling during malaria parasite invasion. *PLoS Biol.* **17**, e3000154

66. Macek, B., Gnad, F., Soufi, B., Kumar, C., Olsen, J. V., Mijakovic, I., and Mann, M. (2008) Phosphoproteome analysis of E. coli reveals evolutionary conservation of bacterial Ser/Thr/Tyr phosphorylation. *Mol. Cell. Proteomics*. **7**, 299–307

67. Deutscher, J., and Saier, M. H. (2006) Ser/Thr/Tyr protein phosphorylation in bacteria - For long time neglected, now well established. *J. Mol. Microbiol. Biotechnol.* **9**, 125–131

68. Mann, N. H. (1984) Protein Phosphorylation in Escherichia coli and Purification of a Protein Kinase. *J. Biol. Chem.* **259**, 526–533

69. Savitski, M. M., Lemeer, S., Boesche, M., Lang, M., Mathieson, T., Bantscheff, M., and Kuster, B. (2011) Confident phosphorylation site localization using the mascot delta score. *Mol. Cell. Proteomics*. 10.1074/mcp.M110.003830

70. Yang, J., Anishchenko, I., Park, H., Peng, Z., Ovchinnikov, S., and Baker, D. (2020) Improved protein structure prediction using predicted interresidue orientations. *Proc. Natl. Acad. Sci. U. S. A.* 10.1073/pnas.1914677117

71. Petoukhov, M. V., Franke, D., Shkumatov, A. V., Tria, G., Kikhney, A. G., Gajda, M., Gorba, C., Mertens, H. D. T., Konarev, P. V., and Svergun, D. I. (2012) New developments in the ATSAS program package for small-angle scattering data analysis. *J. Appl. Crystallogr.* 10.1107/S0021889812007662

72. Shrestha, A., Hamilton, G., O'Neill, E., Knapp, S., and Elkins, J. M. (2012) Analysis of conditions affecting auto-phosphorylation of human kinases during expression in bacteria. *Protein Expr. Purif.* **81**, 136–143

73. Invergo, B. M., Brochet, M., Yu, L., Choudhary, J., Beltrao, P., and Billker, O. (2017) Sub-minute Phosphoregulation of Cell Cycle Systems during Plasmodium Gamete Formation. *Cell Rep.* **21**, 2017–2029

74. Bui, H. T. N., Niederwieser, I., Bird, M. J., Dai, W., Brancucci, N. M. B., Moes, S., Jenoe, P., Lucet, I. S., Doerig, C., and Voss, T. S. (2019) Mapping and functional analysis of

heterochromatin protein 1 phosphorylation in the malaria parasite Plasmodium falciparum. *Sci. Rep.* 10.1038/s41598-019-53325-9

75. Arsène, F., Tomoyasu, T., and Bukau, B. (2000) The heat shock response of Escherichia coli. in *International Journal of Food Microbiology*, 10.1016/S0168-1605(00)00206-3

76. Ilouz, R., Kaidanovich, O., Gurwitz, D., and Eldar-Finkelman, H. (2002) Inhibition of glycogen synthase kinase-3β by bivalent zinc ions: Insight into the insulin-mimetic action of zinc. *Biochem. Biophys. Res. Commun.* 10.1016/S0006-291X(02)00636-8

77. Ryves, W. J., Harwood, A. J., Dajani, R., and Pearl, L. (2002) Glycogen synthase kinase-3 inhibition by lithium and beryllium suggests the presence of two magnesium binding sites. *Biochem. Biophys. Res. Commun.* 10.1006/bbrc.2001.6305

78. Ryves, W. J., and Harwood, A. J. (2001) Lithium inhibits glycogen synthase kinase-3 by competition for magnesium. *Biochem. Biophys. Res. Commun.* 10.1006/bbrc.2000.4169

79. Mudireddy, S. R., Abdul, A. R. M., Gorjala, P., and Gary, R. K. (2014) Beryllium is an inhibitor of cellular GSK-3β that is 1,000-fold more potent than lithium. *BioMetals*. 10.1007/s10534-014-9783-y

80. Marvin, R. G., Wolford, J. L., Kidd, M. J., Murphy, S., Ward, J., Que, E. L., Mayer, M. L., Pennen-Hahn, J. E., Haldar, K., and O'Halloran, T. V. (2012) Fluxes in 'Free' and Total Zinc are Essential for Progression of Intraerythrocytic Stages of Plasmodium falciparum. *Bone*. **19**, 731–741

81. Lolli, G., Pinna, L. A., and Battistutta, R. (2012) Structural determinants of protein kinase CK2 regulation by autoinhibitory polymerization. *ACS Chem. Biol.* **7**, 1158–1163

82. Berrow, N. S., Alderton, D., Sainsbury, S., Nettleship, J., Assenberg, R., Rahman, N., Stuart, D. I., and Owens, R. J. (2007) A versatile ligation-independent cloning method suitable for high-throughput expression screening applications. *Nucleic Acids Res.* 10.1093/nar/gkm047

83. Zhang, Y., Werling, U., and Edelmann, W. (2014) Seamless Ligation Cloning Extract (SLiCE) cloning method. *Methods Mol. Biol.* **1116**, 235–244

84. Birnbaum, J., Flemming, S., Reichard, N., Soares, A. B., Mesén-Ramírez, P., Jonscher, E., Bergmann, B., and Spielmann, T. (2017) A genetic system to study Plasmodium falciparum protein function. *Nat. Methods*. 10.1038/nmeth.4223

85. Burda, P. C., Crosskey, T., Lauk, K., Zurborg, A., Söhnchen, C., Liffner, B., Wilcke, L., Pietsch, E., Strauss, J., Jeffries, C. M., Svergun, D. I., Wilson, D. W., Wilmanns, M., and Gilberger, T. W. (2020) Structure-Based Identification and Functional Characterization of a Lipocalin in the Malaria Parasite Plasmodium falciparum. *Cell Rep.* 10.1016/j.celrep.2020.107817

86. Manavalan, P., and Johnson, W. C. (1987) Variable selection method improves the prediction of protein secondary structure from circular dichroism spectra. *Anal. Biochem.* 10.1016/0003-2697(87)90135-7

87. Sreerama, N., and Woody, R. W. (2000) Estimation of protein secondary structure from circular dichroism spectra: Comparison of CONTIN, SELCON, and CDSSTR methods with an expanded reference set. *Anal. Biochem.* 10.1006/abio.2000.4880

88. Whitmore, L., and Wallace, B. A. (2008) Protein secondary structure analyses from circular dichroism spectroscopy: Methods and reference databases. *Biopolymers*. 10.1002/bip.20853

89. Blanchet, C. E., Zozulya, A. V., Kikhney, A. G., Franke, D., Konarev, P. V., Shang, W., Klaering, R., Robrahn, B., Hermes, C., Cipriani, F., Svergun, D. I., and Roessle, M. (2012) Instrumental setup for high-throughput small-and wide-angle solution scattering at the X33 beamline of EMBL Hamburg. *J. Appl. Crystallogr.* 10.1107/S0021889812013490

90. Graewert, M. A., Franke, D., Jeffries, C. M., Blanchet, C. E., Ruskule, D., Kuhle, K.,

970 Flieger, A., Schäfer, B., Tartsch, B., Meijers, R., and Svergun, D. I. (2015) Automated
971 pipeline for purification, biophysical and X-ray analysis of biomacromolecular solutions.
972 *Sci. Rep.* 10.1038/srep10734
973 91. Franke, D., Petoukhov, M. V., Konarev, P. V., Panjkovich, A., Tuukkanen, A., Mertens,
974 H. D. T., Kikhney, A. G., Hajizadeh, N. R., Franklin, J. M., Jeffries, C. M., and Svergun,
975 D. I. (2017) ATSAS 2.8: A comprehensive data analysis suite for small-angle scattering
976 from macromolecular solutions. *J. Appl. Crystallogr.* 10.1107/S1600576717007786
977 92. Svergun, D., Barberato, C., and Koch, M. H. (1995) CRYSOL - A program to evaluate
978 X-ray solution scattering of biological macromolecules from atomic coordinates. *J. Appl.*
979 *Crystallogr.* 10.1107/S0021889895007047
980 93. Schweda, S. I., Alder, A., and Gilberger, T. 4-Arylthieno[2,3-b]pyridine-2-carboxamides
981 Are a New Class of Antiplasmodial Agents Sandra. *Molecules*
982 94. Trager, W., and Jensen, J. B. (1976) Human malaria parasites in continuous culture.
983 *Science (80-.).* 10.1126/science.781840
984 95. Walliker, D., Quakyi, I. A., Wellems, T. E., McCutchan, T. F., Szarfman, A., London, W.
985 T., Corcoran, L. M., Burkot, T. R., and Carter, R. (1987) Genetic analysis of the human
986 malaria parasite Plasmodium falciparum. *Science (80-.).* 10.1126/science.3299700
987 96. Moon, R. W., Hall, J., Rangkuti, F., Ho, Y. S., Almond, N., Mitchell, G. H., Pain, A.,
988 Holder, A. A., and Blackman, M. J. (2013) Adaptation of the genetically tractable malaria
989 pathogen Plasmodium knowlesi to continuous culture in human erythrocytes. *Proc.*
990 *Natl. Acad. Sci. U. S. A.* 10.1073/pnas.1216457110
991 97. Hughes, C. S., Foehr, S., Garfield, D. A., Furlong, E. E., Steinmetz, L. M., and
992 Krijgsveld, J. (2014) Ultrasensitive proteome analysis using paramagnetic bead
993 technology. *Mol. Syst. Biol.* 10.15252/msb.20145625
994 98. Sridharan, S., Kurzawa, N., Werner, T., Günthner, I., Helm, D., Huber, W., Bantscheff,
995 M., and Savitski, M. M. (2019) Proteome-wide solubility and thermal stability profiling
996 reveals distinct regulatory roles for ATP. *Nat. Commun.* 10.1038/s41467-019-09107-y
997 99. Franken, H., Mathieson, T., Childs, D., Sweetman, G. M. A., Werner, T., Tögel, I., Doce,
998 C., Gade, S., Bantscheff, M., Drewes, G., Reinhard, F. B. M., Huber, W., and Savitski,
999 M. M. (2015) Thermal proteome profiling for unbiased identification of direct and indirect
1000 drug targets using multiplexed quantitative mass spectrometry. *Nat. Protoc.*
1001 10.1038/nprot.2015.101
1002 100. Savitski, M. M., Wilhelm, M., Hahne, H., Kuster, B., and Bantscheff, M. (2015) A
1003 scalable approach for protein false discovery rate estimation in large proteomic data
1004 sets. *Mol. Cell. Proteomics*. 10.1074/mcp.M114.046995
1005 101. R Core Team (2020) (2020) R: A language and environment for statistical computing.
1006 *R A Lang. Environ. Stat. Comput. R Found. Stat. Comput. Vienna, Austria*
1007 102. Rozewicki, J., Li, S., Amada, K. M., Standley, D. M., and Katoh, K. (2019) MAFFT-
1008 DASH: integrated protein sequence and structural alignment. *Nucleic Acids Res.*
1009 10.1093/nar/gkz342
1010 103. Cole, C., Barber, J. D., and Barton, G. J. (2008) The Jpred 3 secondary structure
1011 prediction server. *Nucleic Acids Res.* 10.1093/nar/gkn238
1012 104. Hiranuma, N., Park, H., Baek, M., Anishchenko, I., Dauparas, J., and Baker, D. (2021)
1013 Improved protein structure refinement guided by deep learning based accuracy
1014 estimation. *Nat. Commun.* 10.1038/s41467-021-21511-x
1015 105. Camacho, C., Coulouris, G., Avagyan, V., Ma, N., Papadopoulos, J., Bealer, K., and
1016 Madden, T. L. (2009) BLAST+: Architecture and applications. *BMC Bioinformatics*. **10**,
1017 421
1018 106. Bodenhofer, U., Bonatesta, E., Horejš-Kainrath, C., and Hochreiter, S. (2015) Msa: An
1019 R package for multiple sequence alignment. *Bioinformatics*. **31**, 3997–3999
1020 107. Guindon, S., Dufayard, J. F., Lefort, V., Anisimova, M., Hordijk, W., and Gascuel, O.
1021 (2010) New algorithms and methods to estimate maximum-likelihood phylogenies:

Assessing the performance of PhyML 3.0. *Syst. Biol.* 10.1093/sysbio/syq010

108. Yu, G. (2020) Using ggtree to Visualize Data on Tree-Like Structures. *Curr. Protoc. Bioinforma.* **35**, 3041–3043

109. Drozdetskiy, A., Cole, C., Procter, J., and Barton, G. J. (2015) JPred4: A protein secondary structure prediction server. *Nucleic Acids Res.* 10.1093/nar/gkv332

110. Prommana, P., Uthaipibull, C., Wongsombat, C., Kamchonwongpaisan, S., Yuthavong, Y., Knuepfer, E., Holder, A. A., and Shaw, P. J. (2013) Inducible Knockdown of Plasmodium Gene Expression Using the glmS Ribozyme. *PLoS One*. **8**, e73783

111. Daubenberger, C. A., Tisdale, E. J., Curcic, M., Diaz, D., Silvie, O., Mazier, D., Eling, W., Bohrmann, B., Matile, H., and Pluschke, G. (2003) The N'-terminal domain of glyceraldehyde-3-phosphate dehydrogenase of the apicomplexan Plasmodium falciparum mediates GTPase Rab2-dependent recruitment to membranes. *Biol. Chem.* **384**, 1227–1237

Abbreviations

AMA1	*Plasmodium falciparum* Apical membrane Antigen 1
GSK3β	Glycogen Synthase Kinase beta
IEX	ion exchange chromatography
IMAC	immobilized metal affinity chromatography
high-MW	high molecular weight
PfGSK3	*Plasmodium falciparum* Glycogen Synthase Kinase
SEC	size exclusion chromatography

Table 1. SAXS sample details, data acquisition parameters, structural parameters and atomistic modelling.

Sample details		
Sample	**PfGSK3 – F1**	**PfGSK3 – F4**
Organism	*P. falciparum*	
Source	*E. coli* (DE3) C41	
UniProt ID	O77344	
Extinction coefficient ε (at 280 nm, M^{-1} cm^{-1})	48250	
Molecular weight from chemical composition (Da)	52045.2	
Concentration (analysis or injection, mg/ml)	10	
Solvent composition	20mM Tris pH 8.0, 100mM NaCl, 0.5mM TCEP	
SAS data collection parameters		
Beamline	P12, DESY/EMBL, Hamburg (Germany)	
Detector	Pilatus 6M	
Energy (kEV)	10.0	
Sample-to-detector distance (mm)	3000	
q-measurement range ($Å^{-10}$)	0.003-0.732	
Absolute scaling method	Relative to the scattering of pure water	
Method for monitoring radiation damage	Frame comparison	
Exposed time for frame	900 s (900 x 1 s)	900 s (900 x 1 s)
Mode	SEC-SAXS	SEC-SAXS
Sample temperature (°C)	20	20
Structural parameters		

Guinier analysis		
I(0) (cm^{-1})	0.037±0.001	0.021±0.001
R_g (Å)	34.3±0.4	31.5±0.2
q-range ($Å^{-1}$)	0.01-0.04	0.01-0.04
Fidelity (Quality of fit parameter, *AutoRg*)	0.58	0.98
Molecular weight (kDa)*		
From V_c	66.2	48.7
From *MoW*	86.0	34.1
P(r) analysis		
I(0) (cm^{-1})	0.037±0.001	0.021±0.001
R_g (Å)	35.8±0.01	32.5±0.01
D_{max} (Å)	130±10	115±10
q-range ($Å^{-1}$)	0.01-0.50	0.01-0.25
Total quality estimate	0.62	0.82
Porod volume x 10^3 ($Å^3$)	105	101
Atomistic modelling**	*CRYSOL* with constant subtraction and maximum order of harmonics equal to 50	*CORAL* hybrid rigid body modeling
Structures	Robetta model WLT (4)	
q-range for modelling ($Å^{-1}$)	0.01-0.50	0.01-0.58
χ^2	1.19	1.06
Predicted R_g (Å)	35.3	
Starting crystal structures		Robetta model 3SE (4)
Flexible residues		47-63, 403-440
SASBDB IDs for data and models		
	SASDL77	SASDL87

***** calculated using the appropriate functions in ATSAS (91).

** The values for the best model for each respective dataset are shown.

1049 Figure 1

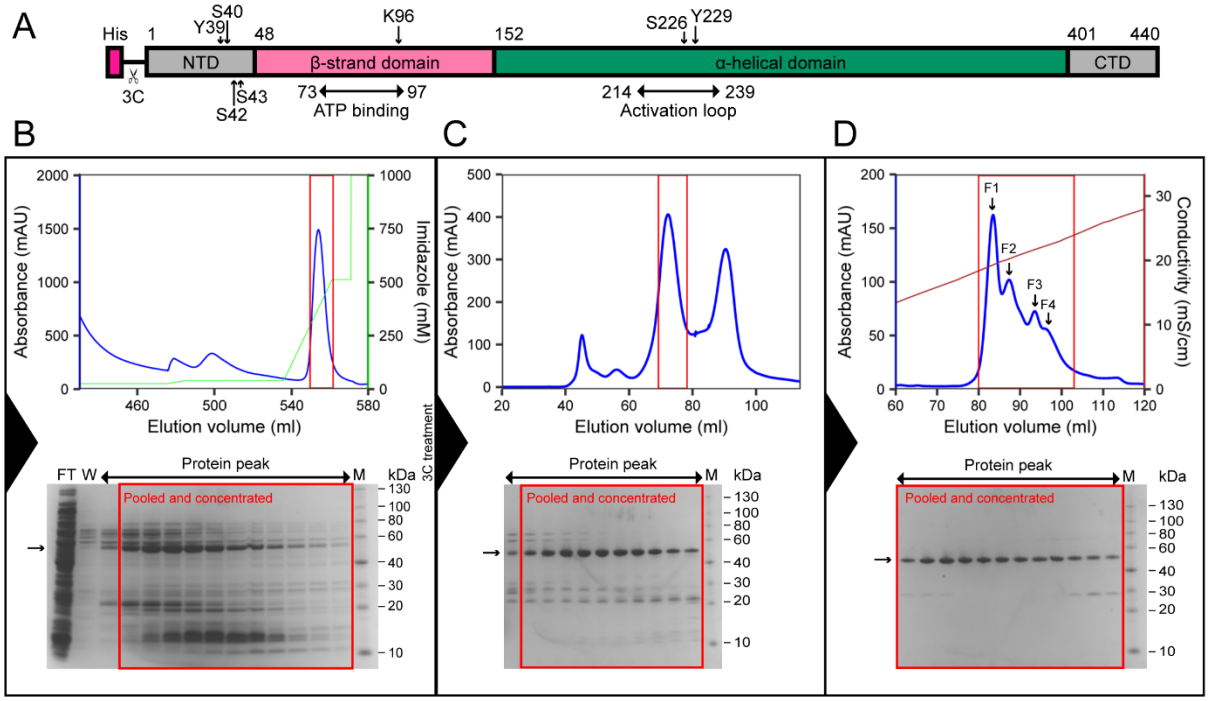

1050

1051 **Fig. 1. Expression and purification of PfGSK3.**

1052 (A) Construct of PfGSK3 used for expression. The construct consists of the full-length
1053 sequence of PfGSK3 with an N-terminal His-tag and a 3C cleavage site. The domain
1054 organization and phosphorylation sites are marked. NTD is the N-terminal domain, CTD is the
1055 C-terminal domain, 3C is the 3C protease cleavage cite. (B) First PfGSK3 purification step:
1056 imidazole gradient elution profile from the His-Trap column. (C) Elution profile from the
1057 Superdex 200 size exclusion column. (D) NaCl gradient elution profile from Resource Q ion
1058 exchange column. The peaks of the ion exchange elution represent fractions that are
1059 phosphorylated to different extent, increasing from F1 to F4. The blue curves in the
1060 chromatograms show UV absorbance, the green curve shows imidazole concentration and
1061 the brown curve shows the conductivity. The peaks in red squares in chromatograms
1062 correspond to the red squares in corresponding SDS-PAGE gels.

1063 Figure 2

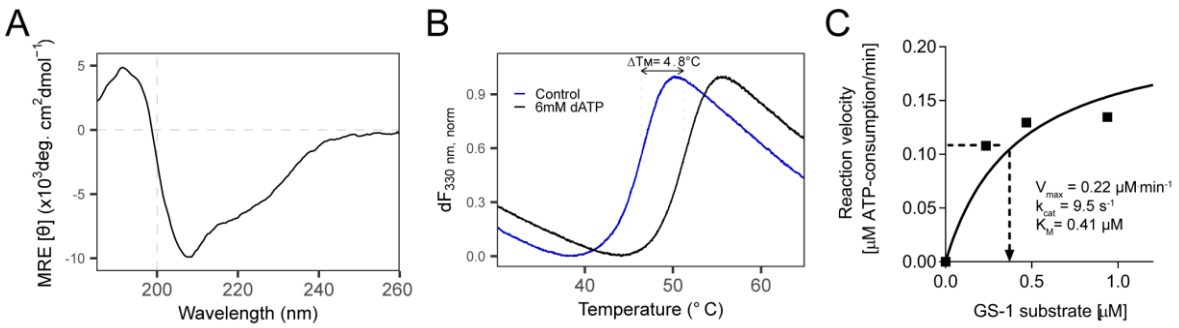

1064

1065 **Fig. 2. Characterization of PfGSK3.**

1066 (A) Circular dichroism shows secondary structure composition similar to what is expected for
1067 a GSK3 protein, with 22% α helix, 26% β sheet, 24% turns and 29% disordered content. The
1068 circular dichroism was measured 10× and the data were averaged, buffer subtracted, and
1069 analyzed by DichroWeb. (B) Thermal unfolding profiles of PfGSK3 in presence or absence of
1070 6mM dATP. dATP stabilizes PfGSK3, suggesting that it binds in the ATP binding pocket. (C)
1071 Catalytic activity of GSK3 follows Michaelis-Menten kinetics. Saturation curve shows the
1072 reaction velocity (as calculated in FigS2F) plotted against different substrate concentrations.
1073 Michaelis-Menten constant (K_m), maximal reaction velocity (V_{max}) and turnover number (k_{cat})
1074 were calculated in GraphPad Prism using nonlinear regression. GS-1 = substrate peptide of
1075 the human glycogen synthase.

Figure 3

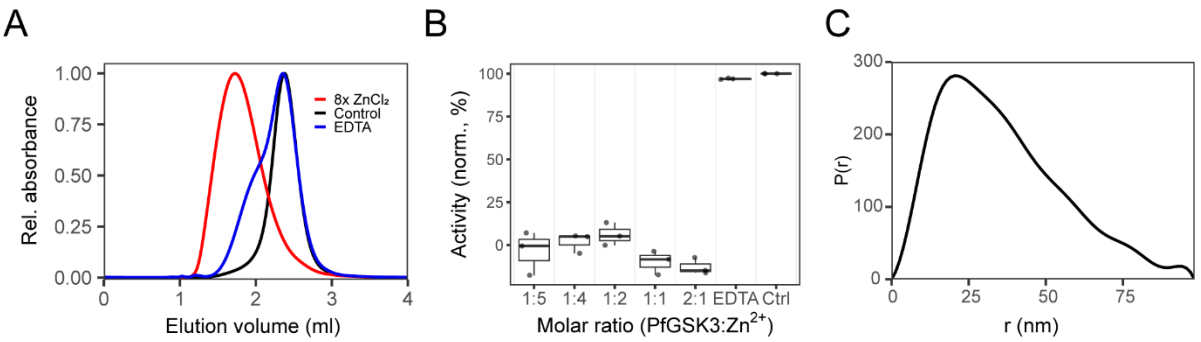

Fig. 3. Heavy metal ions inhibit PfGSK3 activity.

(A) Analytical size exclusion chromatography profiles on a Superose 6 column of PfGSK3 apoprotein (black), after addition of 8× molar excess of zinc chloride (red) and after subsequent addition of EDTA (blue). The analysis shows that zinc ions induce the formation of high-MW PfGSK3 species. The formation is reversible because addition of EDTA shifts the elution profiles towards higher elution volumes. (B) The activity of PfGSK3 is strongly reduced in the presence of zinc ions, whereas the protein regains the activity after the addition of the metal chelator EDTA. (C) The distance distribution of the PfGSK3 high-MW species induced by zinc ions derived from SAXS data shows high heterogeneity in the sample, peaking at 20 nm but with D_{max}=89 nm.

1088 Figure 4

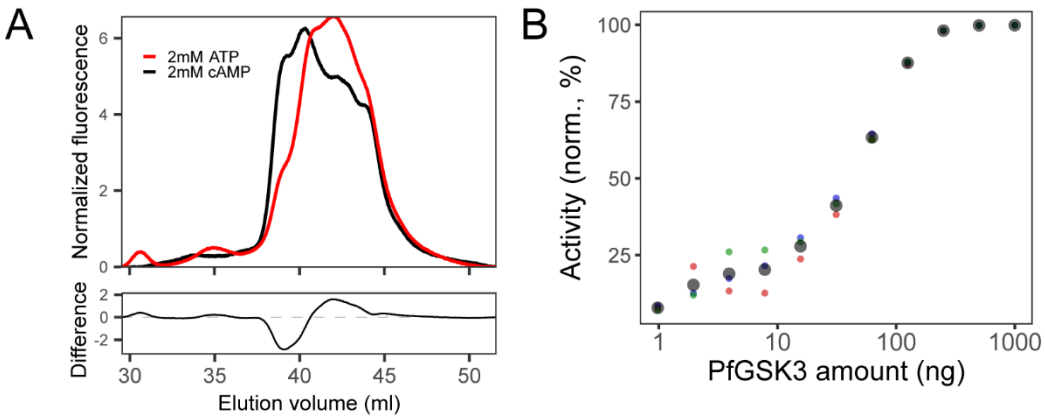

1089

1090 **Fig. 4. PfGSK3 exhibits autophosphorylation.**

1091 (A) IEX elution chromatograms (upper plot) of PfGSK3 after incubation with ATP (red) or cAMP
1092 as negative control (black) in the presence of magnesium ions suggest that PfGSK3 exhibits
1093 autophosphorylation. The difference between both chromatograms (bottom plot) shows an
1094 increase of later-eluting species after ATP treatment, indicating higher amount of
1095 phosphorylation. (B) The ATP consumption measured by the luminescence assay in the
1096 absence of the substrate is dependent on the enzyme concentration, which is indicative of the
1097 autophosphorylation exhibited by PfGSK3.

1098 **Figure 5**

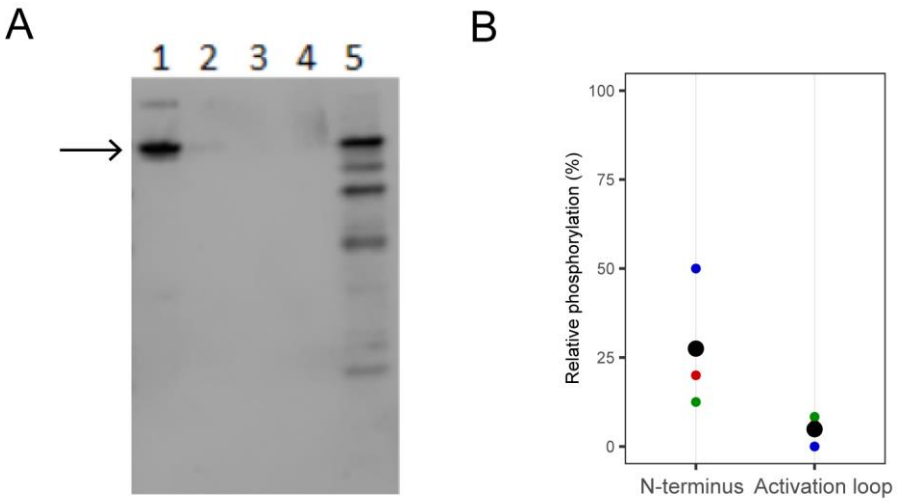

1099

1100 **Fig. 5. N-terminus of PfGSK3 is phosphorylated *in vivo*.**

1101 (A) Western blot with anti-GFP antibodies shows the purification of PfGSK3-GFP from the
1102 plasmodium lysate (1), flow-through (2), two wash steps (3-4) and elution fraction (5). (B) The
1103 mass spectrometry analysis revealed that the N-terminal residues contain higher relative
1104 amount of phosphorylation (27%) compared to the activation loop (5%). The colored points
1105 are ratios from individual mass spectrometry experiment replicates and the large black points
1106 are their averages.

1107 Figure 6

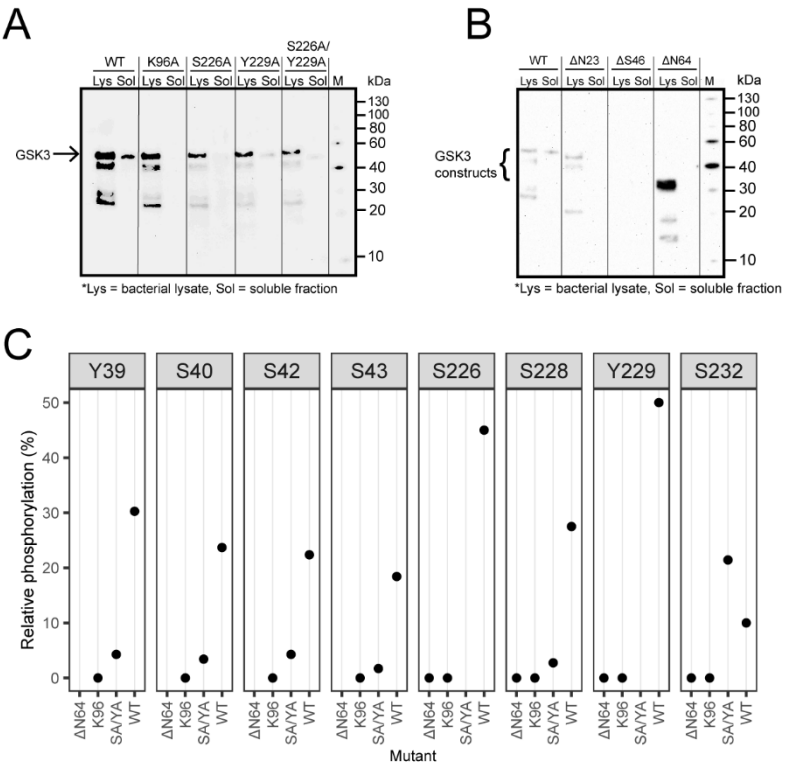

1108

1109 **Fig. 6. The N-terminus and phosphorylation is essential for PfGSK3**

1110 (A) Small-scale expression test of PfGSK3 mutants with inactivating mutations in the ATP
1111 binding site (K96A) and activation loop (Y226A and S229A). Whereas all protein constructs
1112 are expressed, only the wild type PfGSK3 is soluble, which indicates that the
1113 autophosphorylation of PfGSK3 is important for its solubility. (B) Small-scale expression test
1114 of PfGSK3 N-truncated constructs that start with residues N23, S46 or N64. In spite of a very
1115 strong expression of PfGSK3-N64, none of the proteins is soluble, indicating that the PfGSK3
1116 N-terminus is crucial for the autophosphorylation process. The bacterial lysates (Lys) and their
1117 soluble fractions (Sol) were analyzed by Western blot with anti-His antibodies. (C) Analysis of
1118 phosphorylation of PfGSK3 mutants shows that the phosphorylation is completely lost (K96A,
1119 ΔN64) or reduced (S226A/Y229A) compared to the wild-type protein (WT).

Figure 7

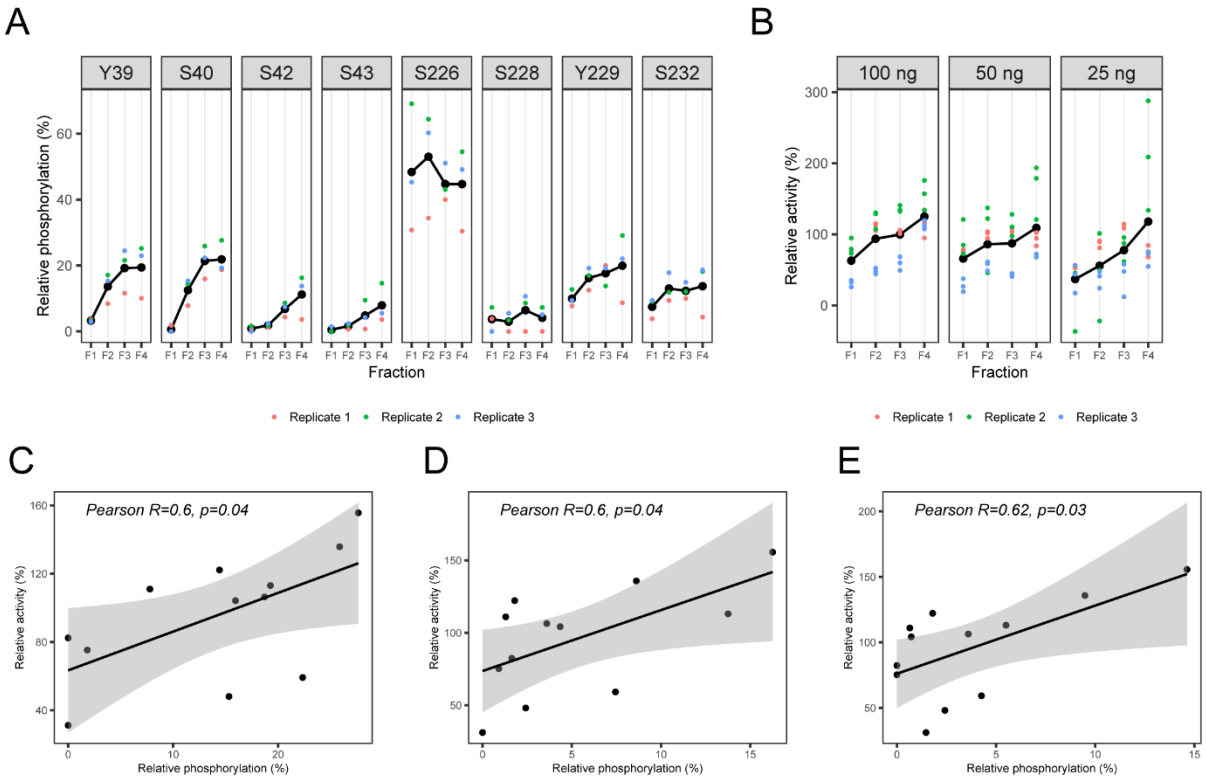

Fig. 7. N-terminal phosphorylation promotes PfGSK3 activity.

(A) Relative phosphorylation of selected residues in the individual PfGSK3 fractions separated by ion exchange chromatography. The relative phosphorylation represents the fraction of all identified residues that were also identified as phosphorylated by LC-MS/MS with Mascot score > 32 and MD score ≥ 5. The data show that the residues in the N-terminal domain are gradually more phosphorylated with increasing IEX elution volume, whereas the phosphorylation at the activation loop remains constant. The different colors represent three biological triplicates. (B) Activity of individual PfGSK3 fractions separated by ion exchange chromatography measured with different PfGSK3 amount (100, 50 and 25 ng). The data show a general trend towards higher activity with increasing phosphorylation in the N-terminal domain. The activity was measured in biological triplicates and at different PfGSK3 concentrations. (C-E) Correlation between the relative phosphorylation of the residues S40, S42 and S43 measured by mass spectrometry, respectively, and the relative activity of the

1135 same samples (triplicates of fractions F1-F4). The data were fitted with a linear model (black

1136 line), the gray background shows the 95% confidence interval.

Figure 8

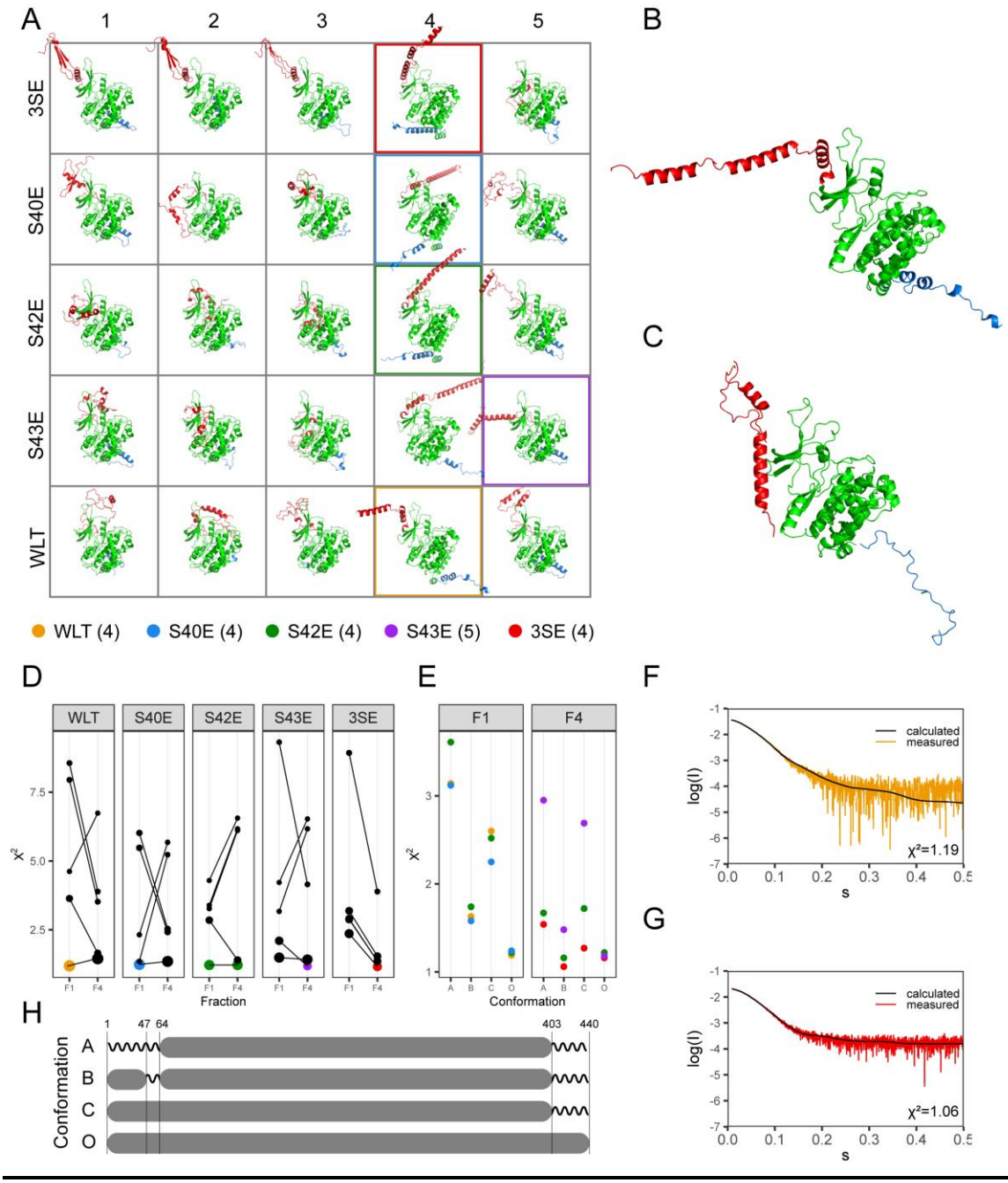

Fig. 8. The N-terminus of PfGSK3 changes the structure upon phosphorylation

(A) Structural models of PfGSK3 predicted by the Robetta server. Five different sequences were used as an input for the prediction and five models were predicted for each sequence. N-termini (residues 1-65) are red, the core domains green and C-termini (residues 403-440) blue. (B) The Robetta model that fits the SAXS data from F1 fraction best display an extended N-terminal helix. (C) The Robetta model refined against SAXS data from fraction F4 using

CORAL with the best fit to the data. The N-terminal helix of this model folds back towards the core of PfGSK3. (D) X^2 values of PfGSK3 structures modelled based on five different sequence modifications (WLT, S40E, S42E, S43E and 3SE) compared to SAXS data recorded for fractions F1 or F4. The identical models are connected with lines. The size of each points correlates with the radius of gyration of the particular model. Three models with lowest X^2 values for each F1 and F4 are colored (see legend). (E) X^2 values of the chosen models refined with CORAL using different strategies, enabling flexibility at either the N-terminus (residues 1-63, strategy A), C-terminus (residues 403-440, strategy C), or at both the C-terminus and residues 47-63 (strategy B). X^2 values of the original models are shown under "O". (F) The SAXS data measured on the PfGSK3 fraction F1 with the fit of theoretical scattering calculated from the best fitting model (X^2=1.19). (G) The SAXS data measured on the PfGSK3 fraction F1 with the fit of theoretical scattering calculated from the best fitting CORAL-refined model (X^2=1.06). (H) Graphical summary of the strategies used for model refinement against SAXS data using CORAL. The gray box symbolizes that the structure of the model was maintained and the zigzag line symbolizes that the structure was replaced with disordered residues by CORAL.